Search for Spatially Extended Fermi-LAT Sources Using Two Years of Flight Data

J. Lande[3],

ABSTRACT

We present a new method for analyzing the spatial extension of sources with the Large Area Telescope (LAT), the primary science instrument on the *Fermi Gamma-ray Space Telescope (Fermi).* The source extension is an important input to correctly associate LAT sources with their counterparts at other wavelengths. We provide a series of Monte Carlo studies to validate this tool and calculate the LAT's detection threshold to spatially extended sources. We then apply this tool to test all sources in the two year source catalog for extension. We present on the detection of nine spatially extended sources in addition to the twelve spatially extended sources reported in the second Fermi-LAT Catalog (2FGL).

*Todo list

---

[3]W. W. Hansen Experimental Physics Laboratory, Kavli Institute for Particle Astrophysics and Cosmology, Department of Physics and SLAC National Accelerator Laboratory, Stanford University, Stanford, CA 94305, USA

1. Introduction

31

32   The Large Area Telescope (LAT) is a pair conversion telescope on the Fermi Gamma-
33 Ray Space Telescope (FGST). It has been surveying the γ-ray sky since June 2008. Fermi
34 has a broad energy coverage (20 MeV to > 300 GeV), wide field of view (~ 2.4sr), and large
35 effective area (~ 8000cm^2 at > 1GeV).

36   Using two years of all sky surveying data, the LAT Collaboration published a catalog
37 of 1873 GeV sourcesAbdo et al. (2011b). Many of these can be positionally associated with
38 a variety of source classes including Active Galactic Nuclei (AGN), pulsars, galaxies, and
39 supernova remnants (SNRs). While many of the LAT sources can be spatially resolved
40 when observed at other frequencies, detection of an extension at GeV energies by the LAT
41 is complicated by the rather large point-spread function (PSF) of the instrument. The
42 angular resolution for events converting in the front part of the detector, defined as the 68%
43 containment radius for a point source, is approximately 3.5° at 100 MeV, improving to about
44 0.1° at 10 GeV.

45   However, a number of sources positionally coincident with LAT sources exhibit extension
46 at other wavelengths which are larger or comparable to the LAT PSF. In particular certain
47 SNRs, pulsar wind nebulae (PWNe), molecular clouds, normal galaxies, galaxy clusters or
48 dark matter satellites can therefore be expected to be observed as spatially extended sources
49 in the LAT. The LAT collaboration has previously reported on the discovered of five spatially

extended supernova remnants, IC443, W28, W44, W51C, and RX J1713.7-3946 (Abdo et al. (2010g,e,f, 2009b, 2011c)). In addition, three extended PWNe were detected: MSH 15-52, Vela X, and HESS J1825-137 (Abdo et al. (2010a); The Fermi LAT Collaboration & Timing Consortium (2010); Grondin et al. (2011)), as well as two close-by galaxies, the Large Magellanic and Small Magalenic Cloud (Abdo et al. (2010h,b)), and finally the radio galaxy Centarus A (Abdo et al. (2010c)) .

For each of these sources, the extension was determined based on dedicated analysis of the particular source or region of interest instead of being the outcome of a systematic search of the LAT catalog. For the systematic scan of all LAT catalog sources presented here, we therefore expect to find additional spatially extended LAT sources, in particular since many extended sources in the Galactic plane have been detected at TeV energies using Air Cherenkov detectors and TeV and GeV emission often originates from the same population of high-energy particles. A variety of spatially extended sources have been detected in the Galactic plane at TeV energies. Most prominent was a survey of the Galactic plane using the High Energy Stereoscopic System (H.E.S.S) which presented 14 spatially extended sources with extensions varying from $0.1°$ to $0.25°$ (Aharonian et al. (2006)). In fact, within our Galaxy only very few sources (most notably the γ-ray binaries LS 5039 (Aharonian et al. (2006a)), LS I+61-303 (Albert et al. (2006); Acciari et al. (2011)) and HESS J0632+057 (Aharonian et al. (2007c)) are amongst the few Galactic sources for which no significant extension was detected at TeV energies. Given these findings, it can be expected that if the source population at GeV energies has similar properties, that at least some of the Fermi-LAT sources in our Galaxy should be spatially resolvable at GeV energies.

Being able to spatially resolve the GeV emission from a source is important for several reasons. Because of the large PSF and the large candidate source density in our Galaxy, source confusion is a severe problem for the identification of LAT sources. Finding a coherent source extension across different energy bands allows a firm association of a LAT source to an otherwise confused counterpart. Because of the strongly varying PSF of the LAT, the spatial and spectral information about a source do not simply decouple. A biased spatial model will bias the spectral model of the source. In particular, performing a spectral analysis on a spatially extended source modeled as point-like will systematically shift the spectral index to be softer. Furthermore, correctly modeling a source's extension is important for improving the model of the sky and removing excess residuals, for example in the region around surrounding the Large Magellanic Cloud (Abdo et al. (2010d)). Additionally, such excess residuals potentially bias the significance and measured spectrum of neighboring sources in the densely populated Galactic plane.

2. Analysis Methods

Morphological studies of sources in the GeV energy range using the LAT are challenging because of the significantly energy-dependent PSF. Additional complications arise close to the Galactic plane due to systematic uncertainties in the Galactic diffuse emission. The LAT's PSF is limited at lower energies by multiple scattering in the tracker and the 68% containment radius of the PSF is approximately 5.1° at 100 MeV when averaged over instrument acceptance and including photons which convert in either the thick or thin layers of the tracker. The PSF improves with energy and approaches a limit given by the granularity of the silicon strips and is 0.14° at 10 GeV (Abdo et al. (2009c)). The high resolution of the higher energy photons in the LAT energy range however is offset by their low statistics. Therefore a detailed investigation has been performed in this work to determine the optimal energy range to measure source extension (see below).

2.1. The *pointlike* Package

A new analysis tool has been developed to address the unique requirements for studying spatially extended sources with the LAT. The tool provides a maximum likelihood analysis where the Poisson likelihood for observing the measured counts is maximized, given a parametrized spatial and spectral model of the source and its surrounding region. The extension of a source can be modeled by a geometric shape (e.g. a disk or Gaussian) and the source's position, extension, and spectrum can be simultaneously fit.

This analysis is not feasible using the standard LAT likelihood analysis tool *gtlike*[1] because *gtlike* can only fit the spectral parameters of the model.

We note that *gtlike* has been used in the past in several studies of source extension in the LAT collaboration (Abdo et al. (2010h,b,e, 2009b)). Based upon a set of *gtlike* maximum likelihood fits at fixed extensions, a profile of the likelihood as a function of the extension was calculated. This approach is not optimal because the position, extension, and spectrum of the source must be simultaneously fit to find the best fit parameters and to correctly compute the statistical significance of the detection. Furthermore since the *gtlike* likelihood profile approach is computationally intensive, no large-scale Monte Carlo effort can be run to validate it.

The approach presented here is based on a second maximum likelihood fitting package

---

[1] *gtlike* is distributed publicly by the Fermi Science Support Center (Fermi Science Support Center (2011))

[115] developed in the LAT collaboration and called *pointlike* (Abdo et al. (2010d); Kerr (2011)).
[116] We extended the code to allow a simultaneous fit of the source extension together with the
[117] position and the spectral parameters.

[118] The choice to base the spatial extension fitting on *pointlike* rather than *gtlike* was made
[119] on considerations of computing time. The *pointlike* algorithm was optimized for speed to
[120] handle larger numbers of sources efficiently which is important for our catalog scan as well
[121] as the Monte Carlo validation of our method. Details on the *pointlike* package can be found
[122] in (Kerr (2011)).

2.2. Extension Fitting

[123]

[124] In *pointlike*, it is assumed that the spatial and spectral model of an extended source are
[125] separable, i.e. that the source model $M(l, b, E) = S(l, b) \times X(E)$. To fit an extended source,
[126] *pointlike* convolves the extended source shape with the PSF (as a function of energy) and uses
[127] the *Minuit* library to maximize the likelihood by simultaneously varying the position and
[128] extension of the source (James & Roos (1975)). As will be described in section 3.1, simul-
[129] taneously fitting the position and extension is necessary to correctly calculate the statistical
[130] significance of the detection of extension. For each position and extension, the spectral pa-
[131] rameters of the sky model are refit. To avoid projection effects, the fitted source position
[132] parameters are not the source's longitude and latitude but instead the source's displacement
[133] in a rotated reference frame.

The significance of the extension of a source can be calculated from $\mathrm{TS_{ext}}$, which is the
test statistic of the likelihood ratio test of a model with a spatially extended source and a
model with a point-like source and defined as

$$\mathrm{TS_{ext}} = 2 \log(LL_{\mathrm{ext}}/LL_{\mathrm{ps}}). \tag{1}$$

[134] where LL is the log of the Poisson likelihood. *pointlike* calculates $\mathrm{TS_{ext}}$ by fitting a source
[135] first with a spatially extended model and then as a point source. The interpretation of $\mathrm{TS_{ext}}$
[136] in terms of a statistical significance is discussed in section 3.1.

For extended sources with an assumed radially symmetric shape, we use a semi-analytic
calculation to speed up the calculation of the expected photon distribution. The expected
photon distribution can be written as

$$\mathrm{PDF}(\vec{r}) = \int \mathrm{PSF}(|\vec{r} - \vec{r}'|) I_{\mathrm{src}}(\vec{r}') dA'. \tag{2}$$

For the LAT, the PSF can be parameterized by a *King function*

$$\text{PSF}(\vec{r}) = \frac{1}{2\pi\sigma^2}\left(1 - \frac{1}{\gamma}\right)\left(1 + \frac{u}{\gamma}\right)^{-\gamma}, \tag{3}$$

where σ and γ are free parameters (Kerr (2011)). For radially symmetric extended sources, the angular part of the integral can be done analytically

$$\text{PDF}(u) = \int_0^\infty \sigma^2 dv I_{\text{src}}(v) \int_0^{2\pi} d\phi' \text{PSF}(\sqrt{2\sigma^2(u + v - 2\sqrt{uv}\cos(\phi - \phi'))}) \tag{4}$$

$$= \int_0^\infty dv I_{\text{src}}(v) \left(\frac{\gamma - 1}{\gamma}\right)\left(\frac{\gamma}{\gamma + u + v}\right)^\gamma \times {}_2F_1\left(\gamma/2, \frac{1 + \gamma}{2}, 1, \frac{4uv}{(\gamma + u + v)^2}\right). \tag{5}$$

137 where $u = (r/\sigma)^2/2$, $v = (r'/\sigma)^2/2$, and ${}_2F_1$ is the Gaussian hypergeometric function. This
138 convolution formula is used by *pointlike*, reducing the calculation of the expected photon
139 distribution to a single numerical integral.

140 There will always be a small numerical discrepancy between the expected photon distri-
141 bution derived from a true point source and a very small extended source due to numerical
142 error in the convolution. In most situations, this error would be insignificant. But in partic-
143 ular for very bright sources, this numerical error has the potential to bias the test statistic
144 for the extension test. the source with an extended shape to the likelihood fitting it with its
145 extension fixed to $10^{-10°}$.

146 We estimate the errors on the extension by recalculating the likelihood for a set of
147 extension values while keeping the position fixed.

148 We estimate the error on the extension of a source by fixing the position of the source
149 and varying the extension until the likelihood has fallen by $\frac{1}{2}$, corresponding to a 1σ error.
150 This method is shown schematically in figure 1(a) which shows the change in LL when
151 varying the extension of the SNR IC443. The localization error is calculated by fixing the
152 extension and spectrum of the source and fitting a Gaussian to the likelihood as a function
153 of position.

2.3. *gtlike* Analysis Validation

155 *pointlike* is important for LAT analysis that require many iterations such as source
156 localization and extension fitting. On the other hand, because of the fewer approximations
157 used in calculating the likelihood we expect the spectral parameters found with *gtlike* to
158 be slightly more precise. Furthermore, because *gtlike* is the standard likelihood analysis
159 package, it has been more extensively validated for spectral analysis. For that reason, in the

following analysis we use *pointlike* to determinate the position and extension of a source and then determine the spectrum using *gtlike*. Both *gtlike* and *pointlike* can be used to estimate the statistical significance of the extension of a source and we require that both methods agree to claim a detection.

We found good agreement between the two methods. For the new extended source candidates, table 5 will shows a comparison of the test statistic TS and $\mathrm{TS_{ext}}$ computed using *pointlike* and *gtlike*. Unless explicitly mentioned, all TS, $\mathrm{TS_{ext}}$, and spectral parameters were calculated using *gtlike* using *pointlike*'s positions and extensions.

2.4. Dual Localization

There is a degeneracy between a spatially extended source and multiple point sources that are separated by angular distances comparable or smaller than the size of the LAT PSF. To assess the possibility of source confusion, we developed a function in *pointlike* to simultaneously fit the position of two point sources.

We define $\mathrm{TS_{inc}}$ as twice the increase in LL fitting the region as two point sources compared to fitting the region as one point source:

$$\mathrm{TS_{inc}} = 2 \times (LL_{\mathrm{2pts}} - LL_{\mathrm{ps}}). \tag{6}$$

$\mathrm{TS_{inc}}$ can not be directly compared to $\mathrm{TS_{ext}}$ to see which model is more significant because the models are not nested (Protassov et al. (2002)). Even though the comparison of $\mathrm{TS_{ext}}$ with $\mathrm{TS_{inc}}$ is not a calibrated test, we find the cases $\mathrm{TS_{inc}} \ll \mathrm{TS_{ext}}$ or $\mathrm{TS_{inc}} \gg \mathrm{TS_{ext}}$ suggestive and we only consider a source to be extended if $\mathrm{TS_{ext}} > \mathrm{TS_{inc}}$.

Like extended sources described in section 2.3, the spectrum of the two point sources can be refit using *gtlike*. We quote the spectral values obtained from *gtlike* using the best fit positions found using *pointlike*. For the extended candidates found by our search, we computed both $\mathrm{TS_{ext}}$ and $\mathrm{TS_{inc}}$. The results will be presented in table 9.

2.5. Comparing Source Sizes

We tested two different models for the spatial shape, either a two dimensional Gaussian

$$I(x,y) = \tfrac{1}{2\pi\sigma^2} \exp\left(-(x^2 + y^2)/2\sigma^2\right) \tag{7}$$

or a uniform disk

$$I(x,y) = \begin{cases} \frac{1}{\pi\sigma^2} & x^2 + y^2 \leq \sigma^2 \\ 0 & x^2 + y^2 > \sigma^2 \end{cases} \tag{8}$$

Although these shapes are significantly different, the convolution of them with the PSF look similar. Figure 2 demonstrates this by showing I_{src}, the PSF, and the PDF for a uniform disk and Gaussian spatial model of size 0.5°.[2] This plot shows that we are not very sensitive to probing the exact structure of an extended source. In the search for extended sources, we therefore use only a uniform disk as our spatial extension shape. We then quote the radius of the disk edge as the size of the source.

3. Validation of Analysis Method

3.1. Significance of Extension

Mattox et al. discuss that the test statistic distribution for a likelihood ratio test on the existence of a source at a given position is Mattox et al. (1996)

$$P(\mathrm{TS}) = \tfrac{1}{2}(\chi_1^2(\mathrm{TS}) + \delta(\mathrm{TS})). \tag{9}$$

The particular form of equation 9 is due to the null hypothesis (source flux $\Phi = 0$) residing on the edge of parameter space and the model hypothesis adding a single degree of freedom. It is plausible to expect a similar distribution of the test statistic in the test for source extension as the same conditions apply (with source flux Φ replaced by source radius r). To validate this claim, we performed a Monte Carlo study to calculate empirical distributions for $\mathrm{TS}_{\mathrm{ext}}$ and compared them to equation 9.

We simulated point sources of varying spectral models using *gtobssim*[3] and fit them them using *pointlike* as both point and extended sources. The point sources were simulated with a power-law spectral model with integrated fluxes above 100 MeV ranging from 3×10^{-9} to $10^{-6}\mathrm{ph/cm^2/s}$ in six discrete steps and spectral indices ranging from 1.5 to 3 in four discrete steps. These values were picked to to represent typical source parameters in LAT-detected sources. The point sources were simulated on top of an isotropic background with an integrated flux above 100 MeV of 1.5×10^{-5} (Sreekumar et al. (1998)). The Monte Carlo

---

[2]To allow a valid comparison between Gaussian and disk shaped morphologies, we define the source size for this test as the radius containing 68% of the intensity (r_{68}). $r_{68,\mathrm{Gaussian}} = 1.51\sigma$ and $r_{68,\mathrm{disk}} = 0.82\sigma$ where σ is defined in equation 7 and equation 8 respectively.

[3]*gtobssim* is distributed by the Fermi Science Support Center (Fermi Science Support Center (2011)).

203 simulation was performed over a one year observation period using a default rocking profile
204 and a representative livetime fraction of 0.8. The reconstruction was performed using 1-100
205 GeV photons and the Pass 7_V6 (P7_V6) Source Instrument Response Function (IRFs).
206 For each point source, we used *pointlike* to fit it as both a point and extended source and
207 calculate TS_{ext} and we only kept the sources which had a significant point source detection
208 (TS > 25).

209   For most of the spectral models, 30,000 statistically independent simulations were per-
210 formed. For the dimmer spectral models, many of the simulations left the source undetected
211 (TS < 25) and were discarded. Table 1 shows the different spectral models used in our study
212 as well as the number of simulations. The cumulative density of TS_{ext} is plotted in figure 3.
213 The $\chi_1^2/2$ distribution of equation 9 is overlaid for comparison.

214   Our Monte Carlo study shows broad agreement between simulations and equation 9.
215 Nevertheless, the agreement is not perfect. It should be noted that the discrepancy seems
216 to be worst for bright sources, a likely cause being numerical errors in the convolution
217 becoming more apparent for sufficiently bright sources. Other possible reasons for departure
218 from equation 9 could be that *pointlike* ignores energy dispersion which would change the
219 PSF's shape as a function of energy. We emphasize that most of the time, our empirical
220 curve lies to the left of the theoretical curve so using the theoretical distribution would lead
221 to an underestimate of the statistical significance of a detection. Therefore, we are confident
222 that $\sqrt{TS_{ext}}$ can be used as a conservative measure of the statistical significance of a source's
223 extension and use it in the following analysis.

4. Extended Source Detection Threshold

225   We calculated the LAT's detection threshold to spatially extended sources. We define
226 the detection threshold as the flux at which the value of TS_{ext} averaged over many statistical
227 representations of a source is $\langle TS_{ext} \rangle = 16$ corresponding to a 4σ detection (see section 3.1).

228   We used the simulation setup described in section 3.1, but instead simulated extended
229 sources with a uniform radially symmetric disk spatial model and instead over the actual
230 two year time interval. For each extension and spectral index, we picked a flux range which
231 bracketed $TS_{ext} = 16$. We then picked ten flux points in this range and repeatedly simu-
232 lated and then performed extension tests of the simulated extended source. We calculated
233 $\langle TS_{ext} \rangle = 16$ by fitting a line to the flux and TS_{ext} values.

234   Figure 4 shows the threshold for sources of four spectral indices from 1.5 to 3 and
235 extension varying from $\sigma = 0.1°$ to $2.0°$. The LAT's threshold to extension is better for

harder sources with more high energy photons and the threshold is best for sources with an extension $\sim 0.5°$ and is significantly worse for very small extended small. Figure 4 shows the threshold using photons with energies between 100 MeV and 100 GeV and also using only 1-100GeV photons. Except for the hardest and largest sources, our detection threshold is almost unchanged when including photons with energies between 100 MeV and 1 GeV. This is also demonstrated in figure 1(b) which shows TS_{ext} for the SNR IC443 computed independently in twelve energy bins between 100 MeV and 100 GeV. For IC443, which has a spectral index ~ 2.4, almost the entire increase in TS comes from energies above 1 GeV. On the other hand, other systematic errors become increasingly important at low energy. For our extension search, we use only only photons with energy above 1 GeV.

Figure 5 shows how the LAT's detection threshold increases with increasing background. We compute the threshold using 1, 10, and 100 times the Sreekumar-like isotropic background. The latter factor approximately represents the intensity of the Galactic diffuse emission near the Galactic center. The figure shows the threshold using 1-100 GeV photons and also using only 10-100 GeV photons. We are less sensitive to extended sources with higher background. Also, given the same flux we are more sensitive to the source if those photons have a higher energies.

Overlaid on figure 5 are the LAT detected extended sources from table 2 and table 3. The extended sources are color coded based upon whether the galactic diffuse and isotropic emission model is closer to 1, 10, or 100 times the Sreekumar-like isotropic spectrum.

Finally, figure 23 shows the LAT's detection threshold for all four spectral indices (1.5, 2, 2.5, and 3) against all three background levels (1, 10, and 100 times the Sreekumar-like isotropic background). For a fixed 1-100 GeV or 10-100 GeV flux, the LAT's detection threshold is only weakly depends upon the spectral index. This effect is most pronounced when using only photons with energies above 10 GeV. The extension thresholds are tabulated in table 6.

5. Extended Source Search Method

2FGL is a list of 1873 GeV sources detected by the LAT. 2FGL included twelve previously published spatially extended sources but did not attempt to fit the extension of these sources. Other than these sources, all 2FGL sources were modeled as point sources and 2FGL did not attempt to resolve the extension of new sources. In this paper, we tested all 2FGL sources for extension to search for new spatially extended GeV sources.

For this search, we build a model of the sky consistent with 2FGL. We used the same

²⁶⁹ two years of data from August 4, 2008 to August 1, 2010 and we used the same Pass 7_V6
²⁷⁰ (P7_V6) Source class event selections and Instrument Response Functions (IRFs, Abdo et al.
²⁷¹ (2011a)). We used the same Galactic diffuse, isotropic diffuse, and earth limb emission model.
²⁷² The spectrum of the Galactic and isotropic diffuse models were refit during the analysis while
²⁷³ the earth limb emission was fixed to it's predicted value.

²⁷⁴ As was shown, we gain little in sensitivity using photons with energies below 1 GeV.
²⁷⁵ On the other hand, the large PSF at low energy makes us more susceptible to systematic
²⁷⁶ errors arising from source confusion due to multiple point sources and susceptible to incorrect
²⁷⁷ modeling of the Galactic diffuse emission. In addition, the Galactic diffuse emission is more
²⁷⁸ pronounced at lower energies due to its steep energy spectrum. For that reason, we performed
²⁷⁹ our search using photons only between 1 GeV and 100 GeV. We used 4 energy bins per each
²⁸⁰ logarithmic decade in energy.

²⁸¹ We also performed a search for extended sources using only 10-100 GeV photons. Even
²⁸² though we are testing the same sources, this approach is complimentary because the Galactic
²⁸³ diffuse emission is even less dominant above 10 GeV. Furthermore, source confusion becomes
²⁸⁴ less of a problem since most LAT sources are not significant at energies above 10 GeV. Using
²⁸⁵ higher energies, we might expect to detect harder sources in more complicated regions. This
²⁸⁶ is beneficial for regions near pulsars which cutoff before 10 GeV and was successfully used
²⁸⁷ in detecting HESS J1825-137 and MSH 15-52 with the LAT (Abdo et al. (2010a); Grondin
²⁸⁸ et al. (2011)).

²⁸⁹ For each catalog source, we tested it for extension using *pointlike* assuming the source
²⁹⁰ had a uniform radially symmetric disk spatial model. We used a circular $10°$ region of
²⁹¹ interest centered on our source and included all catalog sources within $15°$ of the source of
²⁹² interest. We refit the spectral parameters of sources within $2°$ of the source. We modeled
²⁹³ each source with a power-law spectral model. This was reasonable because for a source to be
²⁹⁴ significantly extended, it would have to be fairly hard and fit reasonably well by a power-law.
²⁹⁵ Second, since we began the analysis at either 1 GeV or 10 GeV, we didn't expect there to
²⁹⁶ be significant curvature over this energy range.

²⁹⁷ Finally, when analyzing the region, we automatically removed other 2FGL sources which
²⁹⁸ were within $0.5°$ of the source of interest. This was done because of a concern that extended
²⁹⁹ sources would end up 2FGL as multiple point sources. These spurious sources would then
³⁰⁰ distort the extension fit. For each extended candidate, we performed a dual localization
³⁰¹ procedure (described in section 2.4 to test if the source is extended. We select the sources
³⁰² where $TS_{ext} > 16$.

5.1. Additional Analysis

Since extragalactic sources are typically too far away to be resolvable, we expect most extended sources to be inside our Galaxy and most likely on the Galactic plane. Unfortunately, the GeV emission in the Galactic plane is dominated by extremely structured Galactic diffuse emission. Finding sources on top of this emission is difficult (Abdo et al. (2009a)) as has been discussed in 1FGL and 2FGL (Abdo et al. (2010d, 2011b)). Furthermore, the Galactic plane is crowded and it is often difficult to correctly model nearby sources. Because of this, finding a source with $TS_{ext} > 16$ is not a sufficient criteria for resolving a source. For each extended source, we perform several analysis crosschecks.

As an example of why this is important, we describe the test of 2FGL J1856.2+0450c for extension. Figure 7 shows a Galactic and isotropic diffuse emission subtracted smoothed counts map of this source using 1-100 GeV photons. In this region along the Galactic plane, there appears to be large-scale residual in the diffuse emission. As a result, 2FGL J1856.2+0450c fit to an extension of 1.83° and the result is statistically significant with TS_{ext} =45.4. By looking at the residuals, it is clear that this complicated region is not fit well even though the source's extension is statistically significant. For this reason, we manually discard the extension of this and similar sources.

For each extended source candidate, we took the spatial and spectral model found using *pointlike* and performed a crosscheck by refitting the spectral parameters using *gtlike*. We used a square ROI 14.1° in diameter with 1/32° spatial bins and the same energy binning as *pointlike*. Using *gtlike*, we found a second measure of TS_{ext}, this time not fitting the extension but using a fixed template with the extension determined by *pointlike*. We only considered a source to be significantly extended if *pointlike* and *gtlike* both agreed. For the new extended source candidates, table 5 will show a comparison of of TS_{ext} for *gtlike* and *pointlike*.

For each candidate, we generated a map of residual TS by adding a new source of spectral index 2 into the region and finding the increase in likelihood when fitting its flux. TS maps are useful to look for residual structure in the sky mode. Figure 8 shows a residual TS map for the extended source IC443.

For each candidate, we generated plots of the sum of all counts within a given distance of the source and compared it to the model predictions of a point source. The plots were binned uniformly in $\Delta\theta^2$ so that an isotropic background would be flat. An example radial integral plot is shown for the extended source IC443 in figure 1(c). For each source, we also made Galactic and extragalactic diffuse emission subtracted smoothed counts maps. Figure 1(d) shows an example for IC443.

For each source, we tested to see if the region contained instead multiple point sources by replacing the extended source with two point sources and performed the dual localization procedure described in section 2.4. We only considered a source to be extended if $TS_{ext} >$ TS_{inc}. For the new extended sources, we will show the results of this dual localization in table 9.

Because of the high source density in the Galactic plane, for promising candidates we often had to iteratively improve the model of our background sources to obtain a better fit of the sources. Often, several catalog sources would fill in the emission of the extended source and would have to be removed from the region. Similarly, background sources were often insignificant in the fit energy range and had to be removed. The position of background sources would often have to be refit once the extended source was fit. When the model of the extended source coupled strongly with nearby sources, we iteratively fit the extended source and all nearby sources until the fit converged. For each extended source, we describe the modification that were required.

5.2. Systematic Errors on Extension

We estimate a systematic error on the extension of a source due to uncertainty in our knowledge of the angular resolution of the LAT. Before launch, the LAT PSF was determined by a detector simulation which was verified in accelerator tests (Atwood et al. (2009)). A discrepancy was found in flight data above a few GeV in the PSF compared to the shape of bright AGN. A publication on this issue is in preparation (Abdo et al. (2011a)). Subsequently, the PSF was fit empirically to bright AGN and this empirical parameterization is the default PSF used in the P7_V6 IRFs. To account for this uncertainty in our knowledge of the PSF, we refit our extended source candidates using the Monte Carlo representation of the PSF and consider the difference in extension found using the two PSFs as a systematic error on the extension of a source. Because the Monte Carlo representation of the PSF is smaller, it leads to unphysically higher TS_{ext} values. This same approach was used in (Abdo et al. (2010g)). At high energies, we believe that our parameterization of the PSF from bright AGN is substantially better than the Monte Carlo representation of the PSF so this systematic errors is conservative.

We estimate a second systematic error on the extension of a source due to uncertainty in the model of the Galactic diffuse emission by using an alternative diffuse model. The alternative model was based on the GALPROP[4] model used in the LAT analysis of the

---

[4]GALPROP is a software package for calculating the Galactic γ-ray emission based on a model of cosmic-

isotropic diffuse emission (Abdo et al. (2010i)). With this model, we independently fit along with the point and diffuse sources in the region seven HI rings, seven HII rings, the inverse component, the E(B-V) residual, and the isotropic component of the background emission. All told, we fit in the region 18 diffuse templates. This same crosscheck was used in the LAT Collaboration's analysis of RX J1713.7-3946 (Abdo et al. (2011c)).

It is not expected that this diffuse model is more physical. But adding degrees of freedom to the background model can remove likely spurious sources that correlate with features in the Galactic diffuse emission. Therefore, this tests systematics that may be due to incorrect modeling of the diffuse emission in the region. The results of this fit for the new extended source candidates are shown in table 5. There is good agreement between the TS using the standard and alternative diffuse models, suggesting that the sources are robust against features in the diffuse model.

We do not except the systematic error due to uncertainties in the PSF to be correlated to the systematic due to uncertainty in the Galactic diffuse emission so the total systematic error on the extension of a source so we obtain the total systematic error by adding them in quadrature.

6.   Analysis of Extended Sources in 2FGL

We first present on our analysis of the twelve extended sources included in 2FGL. (Abdo et al. (2011b)). The six extended SNRs IC443, W28, W30, W44, W51C, and the Cygnus Loop were included in 2FGL. IC443, W28, W44, W51C were first reported in (Abdo et al. (2010g,e,f, 2009b)). Detailed papers by the LAT collaboration studying W30 and the Cygnus Loop are still in preparation. GeV emission from W30 was also studied in (Castro & Slane (2010)). Using 1-100 GeV photons, our analysis significantly detected the extension of all six SNRs.

Two nearby galaxies the Large Magalenic Cloud and the Small Magalenic Cloud were included in 2FGL (Abdo et al. (2010h,b)). They were significantly detected using 1-100 GeV photons. Our fit extension is comparable to the published result, but we note that previous publication used a more complicated double Gaussian spatial model when fitting the LMC.

Three pulsar wind nebula Vela X, MSH 15-52, and HESS J1825-137 were included in 2FGL (The Fermi LAT Collaboration & Timing Consortium (2010); Abdo et al. (2010a); Grondin et al. (2011)). Using photons with energy above 10 GeV, we significantly detected

---

ray propagation in the Galaxy. See `http://galprop.stanford.edu/` for details and references

the extension of HESS J1825-137. To improve the model of this source, we removed the nearby catalog source 2FGL J1823.1-1338c which is part of the extended source. To avoid the nearby pulsar PSR J1509-5850, MSH 15-52 must be analyzed at high energies. Using photons with energies above 10 GeV, we fit the extension of MSH 15-52 to be consistent with the published size with an extension significance of $TS_{ext} = 6.5$.

Our analysis was unable to resolve Vela X which would have required first removing the pulsed photons from the Vela pulsar. This is beyond the scope of this paper. Our analysis also failed to detect a significant extension for the Centaurus A Lobes (Abdo et al. (2010c)). This is because the source's emission is significantly more complicated than a uniform radially symmetric Disk.

Our analysis of these sources is summarized in table 2. This table includes the best fit position and extension of these sources when fitting them with a radially symmetric uniform disk spatial model. It also includes the best fit spectral parameters for each source. The position and extension of Vela X and the Centaurus A Lobes are included in this list for completeness.

7. Test of 1LAC Sources

To validate our method, we test associated AGN for extension. GeV emission from AGN is believed to comes from the core of supermassive blackholes in small regions in the core of distant galaxies. Therefore AGN are not expected to be spatially resolvable and provide a good calibration source to demonstrate the efficacy of our tool. Nevertheless, it would be interesting if AGN could be spatially resolved and there are theories that predict this (Aharonian et al. (1994)).

Following 1FGL, the LAT collaboration published a list of sources that had a high probability association with AGN (Abdo et al. (2010j)). 1FGL had 709 1FGL sources associated with 671 distinct AGN at high latitude ($|b| > 10°$). An upcoming publication by the LAT collaboration using two years of data and the 2FGL catalog associates 1017 2FGL sources with AGN. To avoid systematic problems with AGN classification, we selected the 815 AGN which made it into the clean AGN sample. An AGN association is considered clean only if it has a high probability of association $P \geq 80\%$, if it is the only AGN associated with the catalog source, and if there are no flags on the source in 2FGL. These last two conditions are important for our analysis. Source confusion may look like a spatially extended source and flagged catalog sources may correlate with unmodeled structure in the diffuse emission.

Of the 815 clean AGN, we select 775 of these 2FGL sources which are significant above 1

GeV and fit each of them for extension. A histogram of the TS_{ext} values computed for these AGN is shown in figure 9. Overlaid on the plot is the $\chi^2/2$ distribution of equation 9. The TS_{ext} distribution for AGN shows good agreement with the theoretical distribution. Two sources had $TS_{ext} > 9$. One was due to incorrectly pruning a nearby catalog sources and the other was due to a failure of convergence of the point hypothesis. This result demonstrates that we can use TS_{ext} as a measure of the statistical significance of the detection of the extension of a source.

We should clarify that the LAT PSF used in this study was determined empirically by fitting the observed shape of bright AGN (see section 5.2). Finding that the AGN we test are not extended is not surprising. Trying to look for the extension of AGN would require a more specialized analysis.

8. New Extended Sources

Nine extended sources not include in 2FGL were found using this search. Three were found in our search using 1-100 GeV photons and six were found in our search using 10-100 GeV photons. The fit properties of these nine sources is summarized in table 3. This table includes for each source the best fit position, extension, spectrum, source significance, and significance of extension.

For the new extended sources, table 9 presents a test for source confusion by fitting the region as two point sources. The table compares TS_{ext} to TS_{inc} and summarizes the positions and spectra of the two sources. Table 5 contains the fit extensions using the alternate PSF and Galactic diffuse model described in section 5.2.

8.1. 2FGL J0823.0-4246

The two year catalog source 2FGL J0823.0-4246 was found using 1-100 GeV photons to have an extension of $0.37°\pm0.03°$stat$\pm0.02°$sys with an extension significance of $TS_{ext} = 46.3$. The source was fit to a position of $(l, b) = (260.32°, -3.28°)$. Figure 10 shows a counts map of this source. This source is coincident with the one year catalog source 1FGL J0823.3-4248.

To get a good fit of the source, we had to remove the nearby catalog sources 2FGL J0823.4-4305 and 2FGL J0821.0-4254 which are part of the extended source. We tested the source for source confusion by fitting it as two point sources. Because $TS_{inc} = 22.1$ is smaller then TS_{ext}, we conclude that this is an extended source. These modifications are shown in figure 10.

This extended source is spatially coincident with the SNR Puppis A. Overlaid on figure 10 are ROSAT contours of Puppis A (Petre et al. (1996)). There is good agreement between of the X-ray shape with the fit size in GeV.

Add interpretations of Puppis A.

8.2.   2FGL J1627.0-2425c

The two year catalog source 2FGL J1627.0-2425c was found using 1-100 GeV photons to have an extension of $0.41°\pm0.05°$stat$\pm0.02°$sys with an extension significance of $TS_{ext} = 31.1$. The best fit position is $(l, b) = (353.08°, 16.78°)$. This source is coincident with the one year catalog source 1FGL J1628.6-2419c. A counts map showing this source is seen in figure 11. To test for source confusion, we also fit the source instead as two point sources. Since $TS_{inc} = 20.0$ is smaller than TS_{ext}, we conclude that this is an extended source.

This source is in a region of remarkably complicated diffuse emission. Even though it is $16°$ from the Galactic plane, the source is on top of the core of the Ophiuchus molecular cloud which contains massive star-forming regions that are bright in the infrared. We have overlaid on figure 11 contours of the 100 micrometer infared image of this region measured by IRAS. There is good spatial overlap with the GeV emission (Young et al. (1986)).

The region also has abundant molecular and atomic gas traced by CO and HI but also plenty of dark gas, the kind that we find only by its association with dust emission. Embedded star-forming regions make it even more challenging to measure the column density of dust. Although this region is significantly extended, we conclude that this source most likely represents inadequacy in the diffuse γ-ray emission model.

Can we get another citation about dark gas and stuff? And a better description of spectral index being typical of diffuse emission. Stefan says that Markus should write this section. He also says we should cite (Grenier et al. (2005)).

8.3.   2FGL J1712.4-3941

The two year catalog source 2FGL J1712.4-3941 was found using 1-100 GeV photons to have an extnesion $0.56° \pm 0.04°$stat$ \pm 0.02°$sys with an extension significance of $TS_{ext} = 39.6$. This source was fit to a position of $(l, b) = (347.25°, -0.54°)$. The source is coincident with the one year catalog source 1FGL J1711.7-3944c. Figure 12 shows a smoothed counts map

492 of this source.

493 This source is spatially coincident with the SNR RX J1713.7-3946 and was recently
494 reported by (Abdo et al. (2011c)). Figure 12 overlays H.E.S.S. TeV contours of SNR RX
495 J1713.7-3946 from (Aharonian et al. (2007b)). To analyze this source, we used the same
496 background model as the recent LAT publication. 2FGL J1715.4-4024c is spatially coincident
497 with Source A and was moved to $(\mathrm{RA}, \mathrm{Dec}) = (258.84, -40.46)$. Source B was added at
498 $(\mathrm{RA}, \mathrm{Dec}) = (258.71, -38.70)$ and Source C was added at $(\mathrm{RA}, \mathrm{Dec}) = (257.47, -39.75)$.

8.4. 2FGL J0851.7-4635

500 The two year catalog source 2FGL J0851.7-4635 was found using 10-100 GeV photons to
501 have an extension of $1.13° \pm 0.08°\mathrm{stat} \pm 0.05°\mathrm{sys}$ with an extension significance of $\mathrm{TS_{ext}} = 87.2$.
502 The source was fit to a position of $(l, b) = (266.29°, -1.43°)$. Figure 13 shows a counts map
503 of this source.

504 2FGL J0851.7-4635 is spatially coincident with the SNR Vela Jr. Overlaid on figure 13
505 are contours of Vela Jr. as seen in TeV by H.E.S.S (Aharonian et al. (2007a)). The GeV
506 and TeV morphology match well. A detailed papers by the LAT collaboration on Vela Jr.
507 is in preparation.

508 To get a good fit of the source, we had to remove thee nearby catalog sources 2FGL J0853.5-
509 4711, 2FGL J0848.5-4535, and 2FGL J0855.4-4625 which are part of the extended source. In
510 addition, we relocalized the position of the nearby catalog source 2FGL J0854.7-4501 to
511 $(l, b) = (266.24°, 0.49°)$ to better fit its position at high energies in the presence of of the ex-
512 tended source. In addition, we removed the further away catalog sources 2FGL J0858.0-4815
513 and 2FGL J0901.7-4655 because they were not significant above 10 GeV. After modifying
514 the region, we found that $\mathrm{TS_{inc}} = 16.1$ which is less than $\mathrm{TS_{ext}}$ so we conclude that the source
515 is extended These modifications are shown in figure 13.

8.5. 2FGL J1615.0-5051

517 The two year catalog source 2FGL J1615.0-5051 was found using 10-100 TeV photons
518 to have an extension of $0.33° \pm 0.04°\mathrm{stat} \pm 0.01°\mathrm{sys}$ with an extension significance of $\mathrm{TS_{ext}}$
519 $= 16.3$. The source was fit to a position of $(l, b) = (332.38°, -0.14°)$. This source is coincident
520 with the one year catalog source 1FGL J1613.6-5100c. Figure 14 shows a counts map of this
521 source.

This source is less than 1° away from 2FGL J1615.2-5138 which is also spatially extended (see section 8.6). To get a good fit of both sources, we had to model both sources as being spatially extended and iteratively fit the position and extension of each source until obtaining a global best fit. Before doing this, We removed from our model the source 2FGL J1614.9-5212 because it is part of 2FGL J1615.2-5138's. Furthermore, we removed the nearby catalog sources 2FGL J1619.7-5040c and 2FGL J1620.6-5111c because they were not significant above 10 GeV. These modifications are further described in the caption to figure 14. After modifying the region, we found that TS_{inc} =11.9 which is less than TS_{ext} so we conclude that the source is extended.

2FGL J1615.2-5138 is spatially coincident with the extended TeV source HESS J1616-508 (Aharonian et al. (2006)). In figure 14, contours of HESS J1616-508 are overlaid on 2FGL J1615.0-5051. The H.E.S.S. experiment measured a Gaussian extension 0.136 ± 0.008 when fitting the source with an elliptical Gaussian spatial model. This size corresponds to a 68% containment radius of $r_{68} = 0.21° \pm 0.01°$. This size is comparable to the LAT size $r_{68} = 0.27° \pm 0.03°$ (see section 2.5). Figure 18 shows that the LAT spectrum of 2FGL J1615.0-5051 connects smoothly to the H.E.S.S spectrum of HESS J1616-508.

HESS J1616-508 is located in the region of two SNRs, RCW103 (G332.4-04) and Kes 32 (G332.4+0.1) but is not spatially coincident with either of them. HESS J1616-508 is near three pulsars near PSR J1614-5048, PSR J1616-5109, and PSR J1617-5055 but only PSR J1617-5055 only PSR J1617-5055 is energetically favored as being the TeV emitter (Landi et al. (2007a)). Aharonian et al. (2006) speculated that this young pulsar could be responsible for the emission of HESS J1616-508. HESS J1616-508 is 9' away from PSR J1617-5055, which was discovered during ASCA observations of RCW 103 (Torii et al. (1998)). Using an outer gap magnetospheric pulsar model, it was previously predicted to be a TeV emitter (Hirotani (2001)).

The pulsar's position is offset from the maximum of the H.E.S.S emission and would require an asymetric PWNe to power the TeV emission. Offset PWN are expected on theoretical grounds due to the PWNe being crushed by an asymmetric SNR reverse shock (Aharonian et al. (1997); Blondin et al. (2001)) but this makes a possible association more difficult. For HESS J1825-137, the X-ray emission is directed along the TeV offset making this association more compelling.Aharonian et al. (2006b).

In the region around HESS J1616-508, Suzaku found only an upper limit in the 2-10 Kev energy range and suggested this source as an example of a "dark particle accelerator" (Matsumoto et al. (2007)). Landi et al. (2007a) found no evidence of hard X-ray emission in the region of HESS J1616-508 in the 20-100 Kev energy band with the IBIS/ISGRBI on board INTEGRAL. They also observed the field with the XRT on board *Swift* between

0.2-10 Kev and found no compelling source counterpart. Using archival XMM-Newton and BeppoSAX data, they found no plausible X-ray counterpart except for PSR J1617-5055.

Finally, Chandra ACIS observations of PSR J1617-5055 revealed an underlomonous PWN $\sim 1'$ in size around the pulsar (Kargaltsev et al. (2009)). But the PWN is not assymetric towards HESS J1616-508 which casts doubt upon the association.

Note about how it is difficult to explain the TeV to X-ray emission ratio b/c of magnetic field. Refernece in page 7 of (sukazu paper on HESS J1614-518, but it also refers to (Matsumoto et. al 2007 and says this requires small b/field with strong cutoff in eletron energy). Also some not eabout different photon fields being possible.

Note about this this paper finds other stuff: (Kargaltsev et al. (2009)).

The GeV emission is suggested to be the same emission component as the TeV emission, but further observations of this source at other frequencies will likely be needed to firmly associated this source.

Finish interpretations of HESS J1616-508.

8.6.   2FGL J1615.2-5138

The two year catalog source 2FGL J1615.2-5138 was found using 10-100 GeV photons to have an extension of $0.42° \pm 0.03°$stat ± 0.01sys with an extension significance of TS_{ext} =48.0. The source was fit to a position of $(l, b) = (331.66°, -0.66°)$. This source is coincident with the one year catalog source 1FGL J1614.7-5138c. Because 2FGL J1615.2-5138 is close to 2FGL J1615.0-5051, the same model described in section 8.5 was used to analyze both sources. Both sources can be seen in figure 14. For 2FGL J1615.2-5138, TS_{inc} =37.0 which is less than TS_{ext} so we conclude that the source is extended.

This source is spatially coincident with the extended TeV source HESS J1614-518 (Aharonian et al. (2006)). In figure 14, contours of HESS J1614-518 are overlaid on 2FGL J1615.2-5138. The H.E.S.S. experiment measured a Gaussian extension of $\sigma = 0.23° \pm 0.02°$ and $\sigma = 0.15 \pm 0.02$ in the semi-major and semi-minor axis. This size corresponds to a 68% containment size of $r_{68} = 0.35° \pm 0.03°$ and 0.23 ± 0.03. This elliptical size matches the LAT size $r_{68} = 0.35° \pm 0.03°$. Figure 18 shows that the LAT spectrum of 2FGL J1615.2-5138 connects smoothly to the H.E.S.S spectrum of HESS J1614-518. Further data collected by H.E.S.S. in 2007 helped to resolve a double peaked structure in the H.E.S.S. data but no spectral variation across the source, suggesting that the emission is not the confusion of physically

separate sources (Rowell et al. (2008)). The source was also detected by CANGAROO-III (Mizukami et al. (2011)).

This source is currently unidentifed. There are five nearby pulsars, but note are luminous enough to provide the required energy output to power the TeV emission (Rowell et al. (2008)).

HESS J1614-518 is spatially coincident with a young open cluster Pismis 22 (Landi et al. (2007b); Rowell et al. (2008)). GeV and TeV emission could arrise from hadronic acceleration in the winds of massive stars Voelk & Forman (1982); Bednarek (2007). Pisim 22 is at a distance ∼1 kpc and can energetically account for the TeV emission (Rowell et al. (2008)), but it is difficult to explain the difference in size and positional offset between Pismis 22 and HESS J1614-518.

Swift observations

Suzaku observations of the region around HESS J1614-518 reveale three X-ray sources in the region. Suzaku source A is a hard extended source spatially coincident with the peak of HESS J1614-518.

Suzaku source B is in a relativly dim region in the middle of HESS J1614-518 and was not spatially resolvable. source B is spatially coincident with Pisim 22.

Suzaku Source C is a foreground source.

Swift observations the region and resolved six X-ray sources. citation

Emission due to SNR

Emission could be due to a PWN

Emission due to Massive Star

Add interpretations of HESS J1614-518. Stefan says to Suzaku observations.

8.7. 2FGL J1632.4-4753c

The two year catalog source 2FGL J1632.4-4753c was found using 10-100 GeV photons to have an extension of $0.44° \pm 0.04°$stat $\pm 0.03°$sys with an extension significance of $\mathrm{TS_{ext}}$ =64.5. The source was fit to a position of $(l, b) = (336.41°, 0.22°)$. This source is coincident with the one year catalog source 1FGL J1632.9-4802c. Figure 15 shows a counts map of this source.

613   To get a good fit of the source, we had to remove from our model three catalog sources
614 2FGL J1631.7-4720c, 2FGL J1630.2-4752, 2FGL J1634.4-4743c.4-4820c that were part of the
615 extended source.. We then iteratively relocalized the source 2FGL J1635.4-4717c to $(l, b) =$
616 $(337.230°, 0.346°)$ and 2FGL J1636.3-4740c to $(l, b) = (336.968°, -0.066°)$ while fitting the
617 extension of 2FGL J1632.4-4753c. In addition we removed from our model four farther away
618 two year catalog sources 2FGL J1638.0-4703c, 2FGL J1628.1-4857c, 2FGL J1630.1-4615,
619 2FGL J1639.8-4921c because they were not significant above 10 GeV. These modifications
620 are shown in figure 15. To test for source confusion, we compared the likelihood fitting this
621 region as one extended source to the likelihood fitting this region as two point sources. We
622 found $TS_{inc} = 40.6$ which is less than TS_{ext} so we conclude that this is an extended source.

623   This extended source is spatially coincident with the extended TeV source HESS J1632-
624 478 (Aharonian et al. (2006)). In figure 15, contours of HESS J1632-478 are overlaid on
625 2FGL J1635.4-4717c. H.E.S.S measured a Gaussian extension of $\sigma = 0.21 \pm 0.05$ and $0.06 \pm$
626 0.04 along the semi-major and semi-minor axes when fitting the source with an elliptical
627 Gaussian spatial model. This corresponds to a 68% containment size $r_{68} = 0.31° \pm 0.08°$ and
628 0.09 ± 0.06 along the semi-major and semi-minor axis. This size is consistent with the LAT
629 size $r_{68} = 0.36° \pm 0.04°$. Figure 18 shows that the LAT spectrum of 2FGL J1635.4-4717c
630 connects smoothly to the H.E.S.S spectrum of HESS J1632-478 and most likely corresponds
631 to the same emission process

632   Aharonian et al. (2006) argued that this source is positionally coincident with the hard
633 X-ray source IGR J1632-4751 discovered above 15 Kev by the INTEGRAL satellite (Tomsick
634 et al. (2003)). It was also observed by XMM-Newton between 2 and 10 Kev (Rodriguez et al.
635 (2003)) and ASCI between 0.7 and 10 Kev (Sugizaki et al. (2001)). But this X-ray source is
636 suspected to be an galactic X-Ray Binary so the GeV and TeV extension HESS J1632-478
637 and 2FGL J1632.4-4753c disfavors the association.

638   Further observations of the region around HESS J1632-478 by XMM-Newton reveal
639 extended emission between 0.2 Kev and 15 Kev with an elliptical size of $\sim 32''$ and $\sim 15''$
640 in the semi-major and semi-minor axes and inside this extended emission was point-like
641 emission (Balbo et al. (2010)). This x-ray source is positionally coincident with the TeV
642 centroid of the H.E.S.S source. In addition, they used data from MGPS-2, an 843 MHz
643 survey of the galactic plane carried out with the Molonglo Observatory Synthesis Telescope
644 (MOST) to detect an extended diffuse radio source whose size matches well the extended
645 X-ray emission Murphy et al. (2007).

646   They argued that the positional match between the radio and X-ray observations argues
647 for a single synchrotron processes emitting from radio to X-ray. This same source could be
648 responsible for the TeV emission due to inverse Compton and this matches the expected

⁶⁴⁹ emission from a typical PWNe.

⁶⁵⁰ The increased GeV and TeV size compared to the X-ray size has previously been ob-
⁶⁵¹ served in several aging PWNe including HESS J1825-137 (Gaensler et al. (2003); Aharonian
⁶⁵² et al. (2006b), HESS J1640-465 (Aharonian et al. (2006); Funk et al. (2007)), and Vela X
⁶⁵³ (Markwardt & Ogelman (1995); Aharonian et al. (2006c)). This can be explained by a dif-
⁶⁵⁴ ferent synchrotron cooling time for the electroncs producing X-rays and TeV gamma rays.
⁶⁵⁵ Because of the spectral and spatial match between the GeV and TeV emission, the LAT data
⁶⁵⁶ naturally fits into this model as being the rising edge of the inverse Compton component of
⁶⁵⁷ a PWN.

8.8. 2FGL J1837.3-0700c

⁶⁵⁹ The two year catalog source 2FGL J1837.3-0700c was found with 10-100 GeV photons to
⁶⁶⁰ have an extension of $0.35°\pm0.08°$stat$\pm0.03°$sys with an extension significance of $\mathrm{TS_{ext}} = 18.8$.
⁶⁶¹ The source was fit to a position of $(l, b) = (25.08°, 0.13°)$. This source is coincident with the
⁶⁶² one year catalog source 1FGL J1837.5-0659c. Figure 16 shows a counts map of this source.

⁶⁶³ This source is in a complicated region. There are three nearby catalog sources 2FGL J1834.7-
⁶⁶⁴ 0705c, 2FGL J1836.8-0623c, and 2FGL J1839.3-0558c. To get a good fit of 2FGL J1837.3-
⁶⁶⁵ 0700c, we relocalized 2FGL J1834.7-0705c to $(l, b) = (24.77°, 0.50°)$, 2FGL J1836.8-0623c to
⁶⁶⁶ $(l, b) = (25.57°, 0.32°)$, and 2FGL J1839.3-0558c to $(l, b) = (26.08°, 0.23°)$. We removed the
⁶⁶⁷ nearby catalog source 2FGL J1835.5-0649 which is part of the extended source and also the
⁶⁶⁸ farther away catalog source 2FGL J1839.0-0539 because it was not significant above 10 GeV.
⁶⁶⁹ These modifications are shown in figure 16. After modifying the region, we found that $\mathrm{TS_{inc}}$
⁶⁷⁰ $=12.6$ which is less than $\mathrm{TS_{ext}}$, so we conclude that the source is spatially extended.

⁶⁷¹ This source is spatially coincident with the TeV source HESS J1837-069 (Aharonian
⁶⁷² et al. (2006)). In figure 16, contours of HESS J1837-069 are overlaid on 2FGL J1837.3-0700c.
⁶⁷³ H.E.S.S. measured a Gaussian extension of $\sigma = 0.12 \pm 0.02$ and 0.05 ± 0.02 along the semi-
⁶⁷⁴ major and semi-minor axis when fitting the source with an elliptical Gaussian spatial model.
⁶⁷⁵ This corresponds to a 68% containment radius of $r_{68} = 0.18° \pm 0.03°$ and $0.08° \pm 0.03°$
⁶⁷⁶ along the semi-major and semi-minor axis. The size is comparable to LAT which fit a 68%
⁶⁷⁷ containment radius of $r_{68} = 0.29° \pm 0.07°$. The LAT size is larger than the H.E.S.S. size but
⁶⁷⁸ the sizes are almost almost within the 1σ errors. Figure 18 shows that the LAT spectrum of
⁶⁷⁹ 2FGL J1837.3-0700c connects smoothly to the H.E.S.S spectrum of HESS J1837-069.

⁶⁸⁰
Add interpretation of HESS J1837-069.

8.9. 2FGL J2021.5+4026

The two year catalog source 2FGL J2021.5+4026 was found with 10-100 GeV photons to have an extension of $0.59° \pm 0.03°$stat $\pm 0.02°$sys with an extension significance of $TS_{ext} =$ 116.4. The source was fit to a position of $(l, b) = (78.18°, 2.19°)$. This source is coincident with the one year catalog source 1FGL J2020.0+4049. Figure 17 shows a counts map of this source.

To get a good fit of the source, we had to remove the nearby catalog source 2FGL J2019.1+4040 which were part of the extended source. Further, we found it necessary to add an additional point source not in the two year catalog into our background model. The new source is was localized to a position of $(l, b) = (78.85°, 2.67°)$ and had TS = 13.5 . Although the source is not very significant, not including it into the background model appeared visually to significantly throw off the fit of the region. In addition, we removed the four further away catalog sources 2FGL J2022.8+3843c, 2FGL J2020.0+4159, 2FGL J2013.8+4115c, and 2FGL J2012.4+3955c from the region because they were not significant above 10 GeV. After modifying the region, we found that $TS_{inc} =$24.3 which is less than TS_{ext}, so we believe that this source is spatially extended. These modifications are further described in the caption to figure 17.

This source is spatially coincident with the Gamma Cygni SNR. Contours of Gamma Cygni at 408MHz from the Canadian Galactic Plane Survey are overlaid on figure 17 and there is good spatial agreement with the LAT emission (Taylor et al. (2003)).

Add interpretations paragraph. Describe how this source will be more carefully analyzed in "A cocoon of freshly accelerated cosmic rays detected by Fermi in the Cygnus superbubble"

9. Discussion

2FGL reported on the detection of twelve spatially extended sources. Using two years of LAT data and a new analysis method, we present on the detection of nine additional extended sources. We also reanalyze the spatial shape of the extended sources in 2FGL. Finding a coherent source extension with different frequencies, especially at TeV energies, allows us to identify the LAT source. Even still, for many extended LAT sources the source class and emission process is still uncertain.

The position of the 21 extended LAT sources is plotted in figure 19. Most of them lie along the galactic plane. This is expected because extragalactic sources are typically too far

away to be resolvable and most Galactic sources lie along the plane.

Figure 22 shows a comparison of the spectral index of LAT detected extended sources and of all sources in 2FGL. This, and table 2 and 3, show that the LAT observes a population of hard (index < 2) extended sources above 10 GeV which connects to TeV sources. Figure 18 shows the LAT energy spectrum of four of the extended sources which were first discovered in the H.E.S.S. Galactic plane survey (Aharonian et al. (2006)) and have a matching size to LAT extended sources. The LAT energy spectrum connects smoothly to TeV. This is also true of HESS J1825-137 (**??**) and RX J1713.7-3946 (Abdo et al. (2011c)). We conclude that the GeV and TeV emission from these sources is coming from the same emission mechanism.

For the LAT extended sources also seen in TeV, figure 20 shows a comparison of their sizes. There is a good correlation between the GeV and TeV sizes of the sources. Even so, the size of PWNe are expected to vary across the GeV and TeV energy range and the size of HESS J1825-137 was seen by H.E.S.S. to vary between 200 GeV and 20 TeV (The H. E. S. S Collaboration: S. Funk et al. (2007)). HESS J1825-137 is significantly larger in GeV than TeV (Grondin et al. (2011)). It is interesting to compare the GeV and TeV size of other PWN candidates, but definitively measuring this effect would require a more careful analysis of the LAT data using the same elliptical spatial model.

Figure 21 compares the size of the 21 extended LAT sources to the 42 extended H.E.S.S. sources. Because of the large field of view and all sky coverage, the LAT can more easily measure larger sources including the LMC and SMC. On the other hand, the smaller angular resolution of Air Cherenkov detectors allows them to measure a population of extended sources below our sensitivity limit (currently at about $\sim 0.2°$). Fermi has a five year nominal livetime with a goal of ten years of operation. With increased exposure, the LAT will likely begin to resolving these smaller TeV sources. As figure 6 showed, our sensitivity to these smaller sources will will acutally improve faster than $\sqrt{t}$.

REFERENCES

Abdo, A. A., et al. 2009a, Physical Review Letters, 103, 251101

—. 2009b, ApJ, 706, L1

—. 2009c, Astroparticle Physics, 32, 193

—. 2010a, ApJ, 714, 927

—. 2010b, A&A, 523, A46+

742 —. 2010c, Science, 328, 725

743 —. 2010d, ApJS, 188, 405

744 —. 2010e, ApJ, 718, 348

745 —. 2010f, Science, 327, 1103

746 —. 2010g, ApJ, 712, 459

747 —. 2010h, A&A

748 —. 2010i, Physical Review Letters, 104, 101101

749 —. 2010j, ApJ, 715, 429

750 —. 2011a, Astroparticle Physics, in preparation

751 —. 2011b, Pending

752 —. 2011c, ApJ, 734, 28

753 Acciari, V. A., et al. 2009, ApJ, 698, L133

754 —. 2011, ArXiv e-prints

755 Aharonian, F., et al. 2005, A&A, 435, L17

756 —. 2006a, A&A, 460, 743

757 —. 2006b, A&A, 460, 365

758 —. 2006c, A&A, 448, L43

759 Aharonian, F., et al. 2006, Astrophys. J., 636, 777

760 Aharonian, F., et al. 2007a, ApJ, 661, 236

761 —. 2007b, A&A, 464, 235

762 —. 2008, A&A, 481, 401

763 Aharonian, F. A., Atoyan, A. M., & Kifune, T. 1997, MNRAS, 291, 162

764 Aharonian, F. A., Coppi, P. S., & Voelk, H. J. 1994, ApJ, 423, L5

765 Aharonian, F. A., et al. 2007c, A&A, 469, L1

Albert, J., et al. 2006, Science, 312, 1771

Atwood, W. B., et al. 2009, ApJ, 697, 1071

Balbo, M., Saouter, P., Walter, R., Pavan, L., Tramacere, A., Pohl, M., & Zurita-Heras, J.-A. 2010, A&A, 520, A111+

Bednarek, W. 2007, MNRAS, 382, 367

Blondin, J. M., Chevalier, R. A., & Frierson, D. M. 2001, ApJ, 563, 806

Castro, D., & Slane, P. 2010, ApJ, 717, 372

Fermi Science Support Center. 2011, FSSC, `http://fermi.gsfc.nasa.gov/ssc/`

Funk, S., Hinton, J. A., Pühlhofer, G., Aharonian, F. A., Hofmann, W., Reimer, O., & Wagner, S. 2007, ApJ, 662, 517

Gaensler, B. M., Schulz, N. S., Kaspi, V. M., Pivovaroff, M. J., & Becker, W. E. 2003, ApJ, 588, 441

Grenier, I. A., Casandjian, J.-M., & Terrier, R. 2005, Science, 307, 1292

Grondin, M. ., et al. 2011, ArXiv e-prints

Hirotani, K. 2001, ApJ, 549, 495

James, F., & Roos, M. 1975, Comput. Phys. Commun., 10, 343

Julian Krause, E. C., & on behalf of MAGIC, I. R. 2011 (Presented at the 2011 Fermi Symposium, Rome Italy)

Kargaltsev, O., Pavlov, G. G., & Wong, J. A. 2009, The Astrophysical Journal, 690, 891

Kerr, M. 2011, PhD in physics, University of Washington

Landi, R., de Rosa, A., Dean, A. J., Bassani, L., Ubertini, P., & Bird, A. J. 2007a, MNRAS, 380, 926

Landi, R., Masetti, N., Bassani, L., Cellone, S. A., Romero, G. E., Ubertini, P., & Dean, A. J. 2007b, The Astronomer's Telegram, 1047, 1

Markwardt, C. B., & Ogelman, H. 1995, Nature, 375, 40

Matsumoto, H., et al. 2007, PASJ, 59, 199

Mattox, J. R., et al. 1996, ApJ, 461, 396

Mizukami, T., et al. 2011, ArXiv e-prints

Murphy, T., Mauch, T., Green, A., Hunstead, R. W., Piestrzynska, B., Kels, A. P., & Sztajer, P. 2007, MNRAS, 382, 382

Petre, R., Becker, C. M., & Winkler, P. F. 1996, ApJ, 465, L43+

Protassov, R., van Dyk, D. A., Connors, A., Kashyap, V. L., & Siemiginowska, A. 2002, ApJ, 571, 545

Rodriguez, J., Tomsick, J. A., Foschini, L., Walter, R., Goldwurm, A., Corbel, S., & Kaaret, P. 2003, A&A, 407, L41

Rowell, G., Horns, D., Fukui, Y., & Moriguchi, Y. 2008, in American Institute of Physics Conference Series, Vol. 1085, American Institute of Physics Conference Series, ed. F. A. Aharonian, W. Hofmann, & F. Rieger, 241–244

Sreekumar, P., et al. 1998, The Astrophysical Journal, 494, 523

Sugizaki, M., Mitsuda, K., Kaneda, H., Matsuzaki, K., Yamauchi, S., & Koyama, K. 2001, ApJS, 134, 77

Taylor, A. R., et al. 2003, AJ, 125, 3145

The Fermi LAT Collaboration, & Timing Consortium, P. 2010, ArXiv e-prints

The H. E. S. S Collaboration: S. Funk, Hinton, J. A., & deJager, O. C. 2007, ArXiv e-prints

The H.E.S.S. Collaboration. 2011, The H.E.S.S. Source Catalog, http://www.mpi-hd.mpg.de/hfm/HESS/pages/home/sources/

Tomsick, J. A., Lingenfelter, R., Walter, R., Rodriguez, J., Goldwurm, A., Corbel, S., & Kaaret, P. 2003, IAU Circ., 8076, 1

Torii, K., et al. 1998, ApJ, 494, L207+

Voelk, H. J., & Forman, M. 1982, ApJ, 253, 188

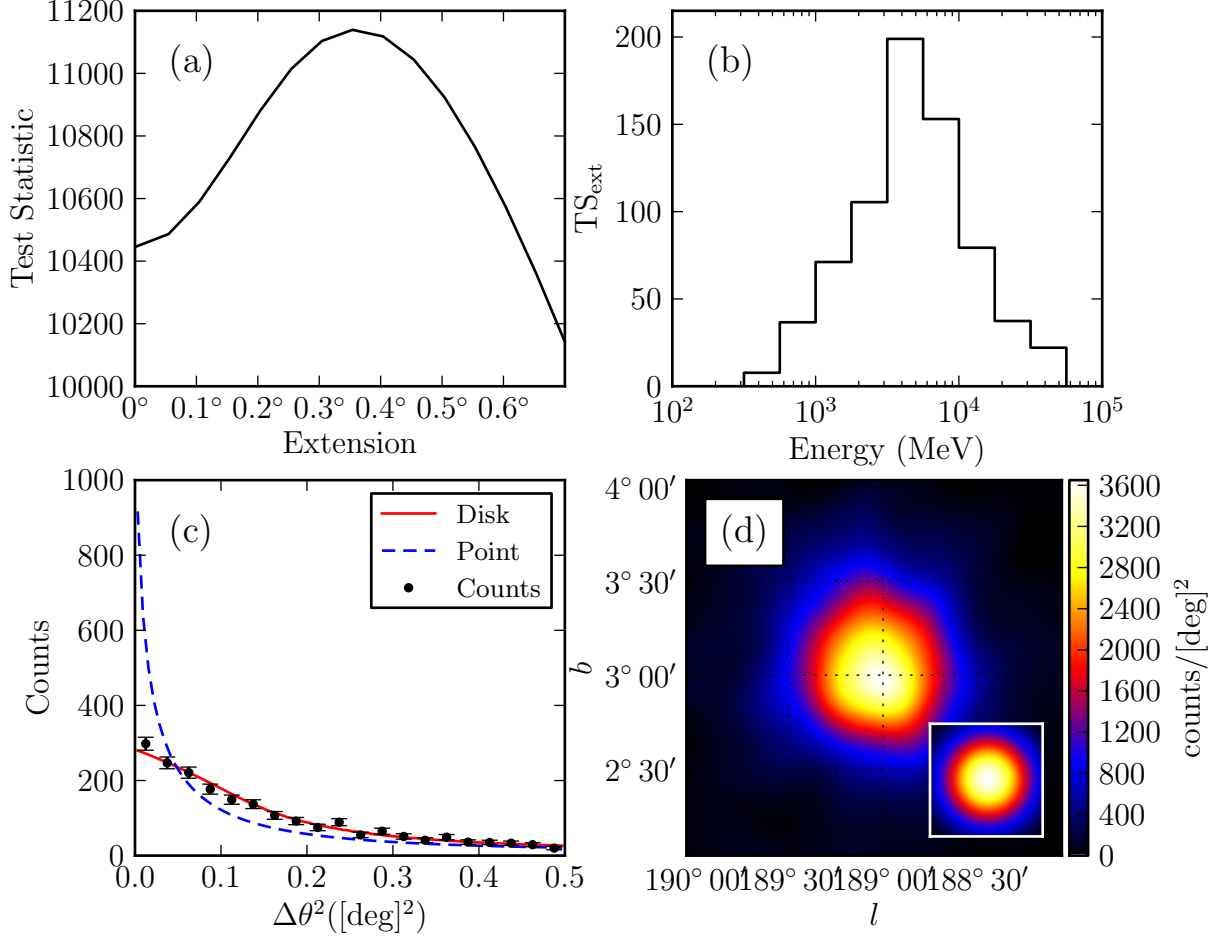Young, E. T., Lada, C. J., & Wilking, B. A. 1986, ApJ, 304, L45

Fig. 1.— All plots are for the SNR IC443 using two years of data. Plot (a) is the change in TS when varying the extension of the source. Plot (b) is TS_{ext} in twelve energy bins. This plot shows that there is little gain in sensitivity to the extension using photons with energies below 1 GeV, even for a source with an index ~ 2.4. Plot (c) is the sum of all counts within a given radial distance from the source binned uniformly in θ^2. Overlaid on the plot is the model predicted counts assuming that the source is both an extended source and a point source Plot (d) is a counts map of the source with the Galactic and isotropic diffuse emission subtracted and smoothed by a $0.1°$ Gaussian kernel. The inset is the predicted emission from a point source of the same spectrum and intensity. The PSF is smoothed by the same kernel. Plots (a), (c), and (d) use only 1-100 GeV photons. Plots (c) and (d) use only photons which converted in the front part of the detector and have an improved angular resolution.
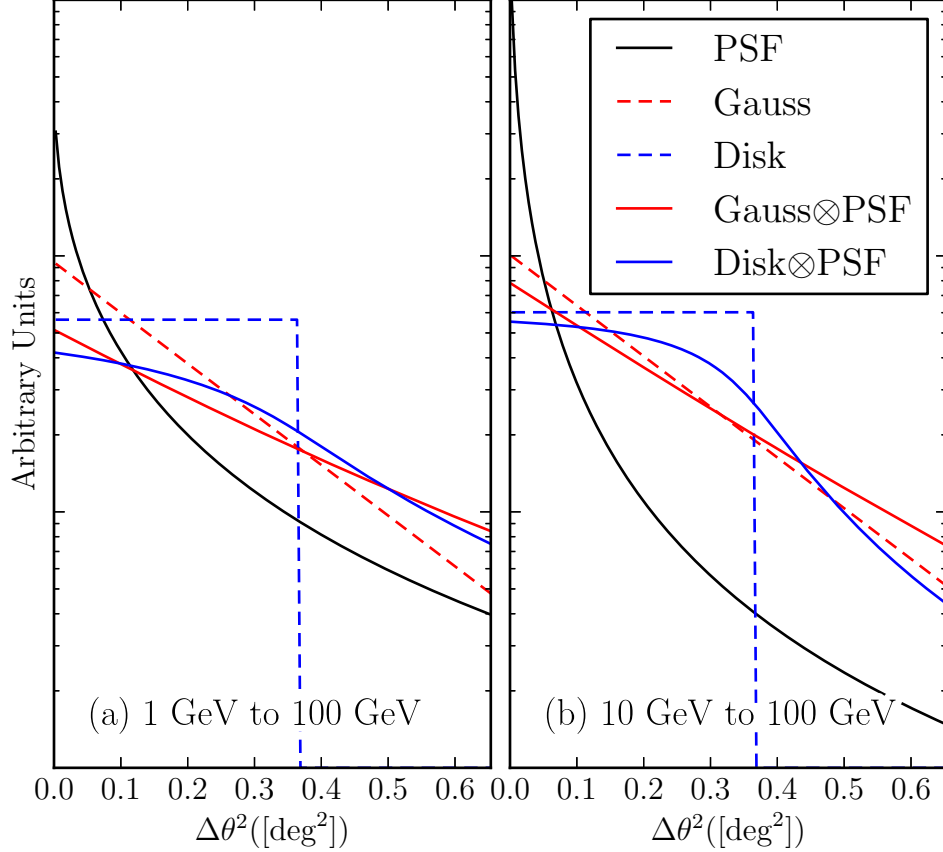
Fig. 2.— A comparison of the Gaussian and uniform disk PDFs before and after convolving with the PSF. The black line is the PSF that would be observed for a power-law source of spectral index 2. The dashed red line is the probability density of a Gaussian with $r_{68} = 0.5°$, which is just a straight line on this plot. The dashed blue line is the probability density for a uniform disk with $r_{68} = 0.5°$. Finally, the solid red and blue lines show the convolution of the Gaussian and uniform disk with the PSF. Plot (a) uses a 1-100 GeV energy range while plot (b) uses a 10-100 GeV enregy range. This plot demonstrates that different spatial models when smoothed by the PSF look similar. The y axis is the log of the intensity and the x axis is θ^2. This plot is discussed further in section 2.5.

γ	flux (ph/cm^2/s)	N_{sims}	$\langle \text{TS} \rangle$
1.5	10^{-6}	31952	92862
	3×10^{-7}	31962	22169
	10^{-7}	31977	5806
	3×10^{-8}	31991	1270
	10^{-8}	31940	301
	3×10^{-9}	30324	62
2	10^{-6}	31872	22067
	3×10^{-7}	31890	4898
	10^{-7}	31858	1097
	3×10^{-8}	31632	236
	10^{-8}	27491	103
2.5	10^{-6}	31822	4706
	3×10^{-7}	31822	889
	10^{-7}	31169	176
	3×10^{-8}	21591	41
3	10^{-6}	31763	929
	3×10^{-7}	31665	161
	10^{-7}	19271	40

Table 1: This table presents a list of the spectral models (flux and spectral index) used in the Monte Carlo study of *pointlike* described in section 3.1 and presented in figure 3. For each spectral model, the number of statistically independent simulations and the average value of TS value ($\langle \text{TS} \rangle$) is tabulated. The Monte Carlo simulation spans parameters representative of sources that could be detected by the LAT. The simulation is of spectral indices γ of 1.5, 2, 2.5, and 3. The simulation is of fluxes varying from a 5σ source detection to a $> 10\sigma$ source detection. Only simulations which produced statistically significant detections (TS > 25) were kept. What is quoted is the > 100 MeV integral flux measured in units of ph/cm^2/s. More information about this Monte Carlo analysis is presented in section 3.1.
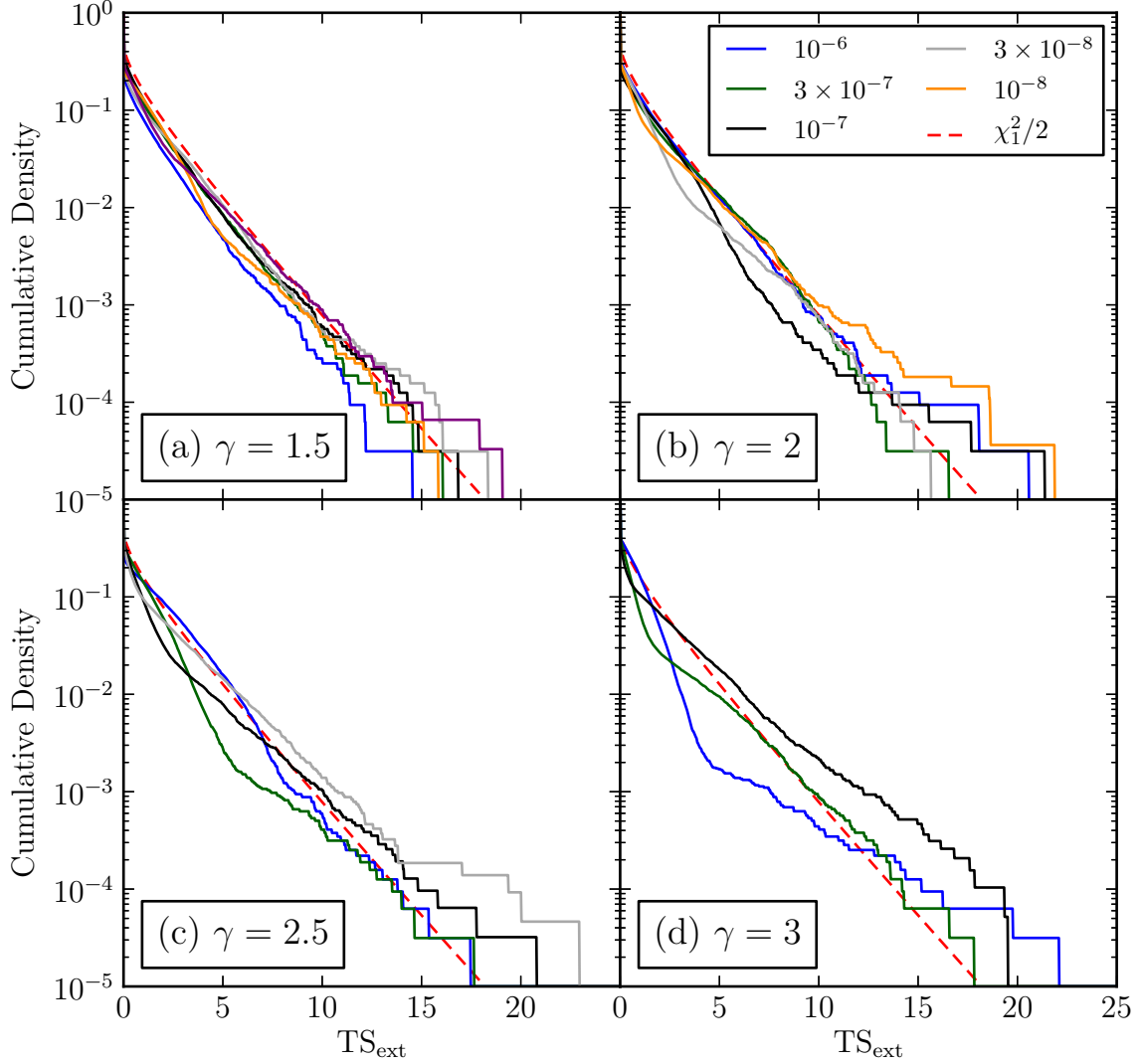
Fig. 3.— The plot shows the null distribution of the likelihood ratio test when fitting a point source for extension. The x axis is TS_{ext} and the y axis is the cumulative density for TS_{ext} of simulated point sources. The four plots represent different spectral indices and the different colors represent different fluxes. The dashed red line is the cumulative density function of $\chi^2(TS)/2$ which is suggested by Wilks' theorem as the distribution these curves should should follow. There is good agreement between the Monte Carlo results and the theoretical distribution. For most spectral parameters, the Monte Carlo curve lies to the left of the theoretical curve which would make the theoretical distribution more conservative. In this paper, we use this theoretical curve to estimate the significance of the detection of a source's extension. This plot cuts off three simulations with $TS_{ext} > 25$. They had a flux 3×10^{-8}ph/cm^2/s, spectral index 2.5, and TS_{ext} of 26.1, 28.9, and 38.1. The Monte Carlo simulation is described in section 3.1 and the number of simulation for each spectral model are presented in table 1.
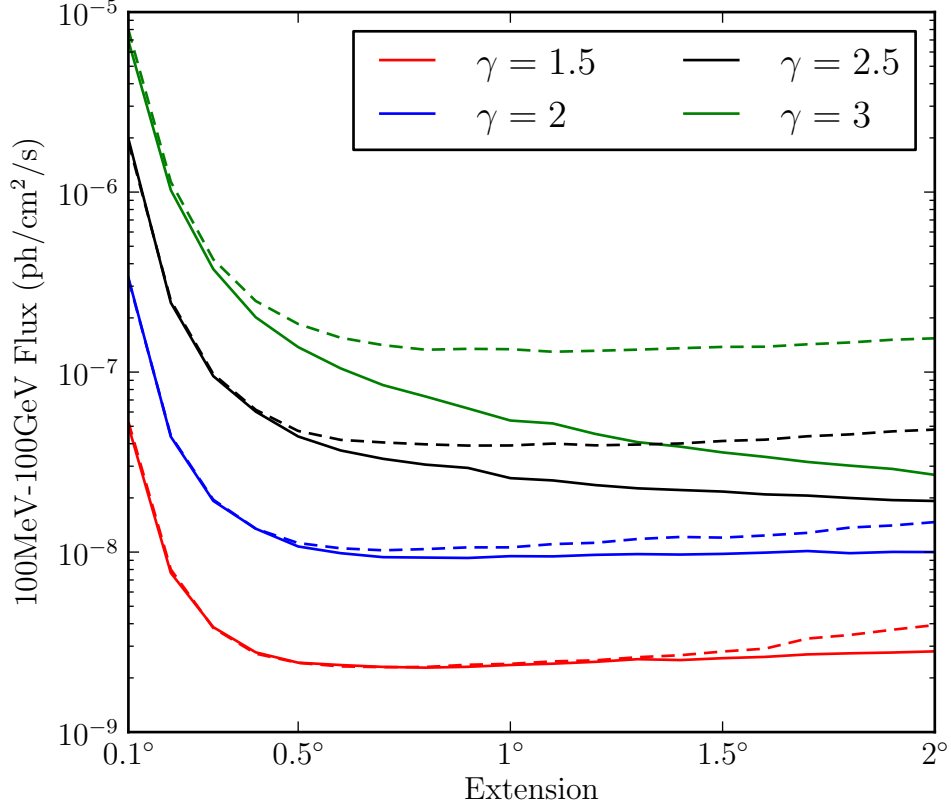
Fig. 4.— This plot shows the detection threshold to resolve a uniform disk extended source. The detection threshold is defined as the flux where $\langle \mathrm{TS_{ext}} \rangle = 16$ for a given extension. The x axis is the extension of a uniform disk extended source and the y axis is the source's 100 MeV to 100 GeV photon flux. All sources have an assumed power-law spectrum and the different colors are different simulated spectral indices. The solid line is the detection threshold using photons with energy between 100 MeV and 100 GeV while the dashed line is the threshold using 1-100 GeV photons. The detection threshold is for the same two year time range as was used in 2FGL and in the following extended source search. The extended sources are simulated against a Sreekumar-like isotropic background. More information about this plot is presented in section 4. This plot shows that our threshold to detecting the extension of a source is best for a source with size 0.5°. It also shows that for sources neither too large nor soft, our sensitivity is not significantly improved using photons with energy between 100 MeV and 1 GeV. More information about this plot is presented in section 4.
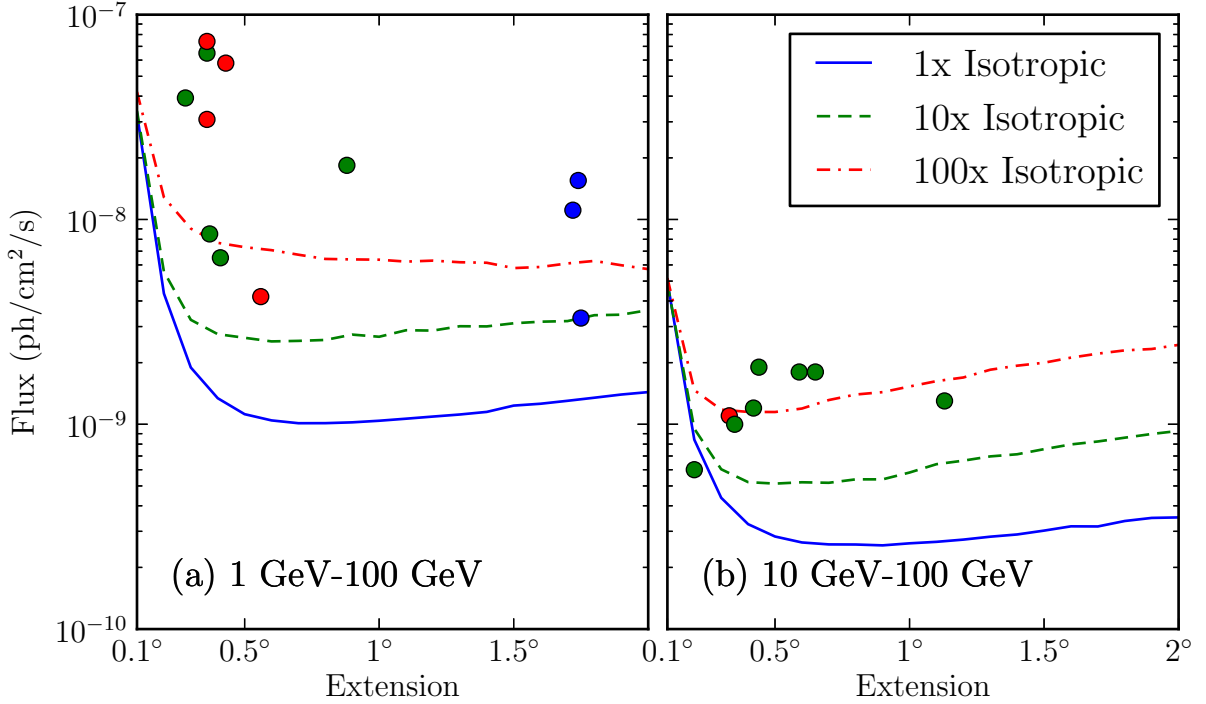
Fig. 5.— This shows the detection threshold to a uniform disk extended source for varying background levels and energy ranges. The plots have the same meaning as in figure 4 and the simulations occur over the same time range. The solid blue line is the detection threshold against a Sreekumar-like isotropic background. The green dashed curve is the threshold against 10 times the isotropic background and the dash dotted red curve is the threshold against 100 times the isotropic background. The latter factor approximately represents the intensity of the Galactic diffuse emission near the Galactic center. Plot (a) is the threshold using 1-100GeV photons while plot (b) is the threshold using 10-100GeV photons. Unlike figure 4, the detection threshold was calculated only for a power-law source of spectral index 2. The flux is quoted only in the selected energy range which weakens the dependence of the detection threshold on spectral index. These plots show that we are less sensitive to extended sources in regions with higher background and (given the same number of photons) more sensitive to harder sources. Overlaid on this plot are the extended sources found in this extended source search. The extended sources are color coded based upon whether the integral galactic diffuse and isotropic diffuse emission model is closer to 1x, 10x, or 100x the Sreekumar-like isotropic spectrum. The red point in plot (a) below the red line is RX J1713.7-3946 which is harder ($\gamma \sim 1.5$) and has diffuse emission only 53 times larger than the isotropic emission. The green point in plot (b) below the green line is MSH 15-52 which was found by our analysis to have $\mathrm{TS_{ext}} = 6.5$. More information about this plot is presented in section 4.
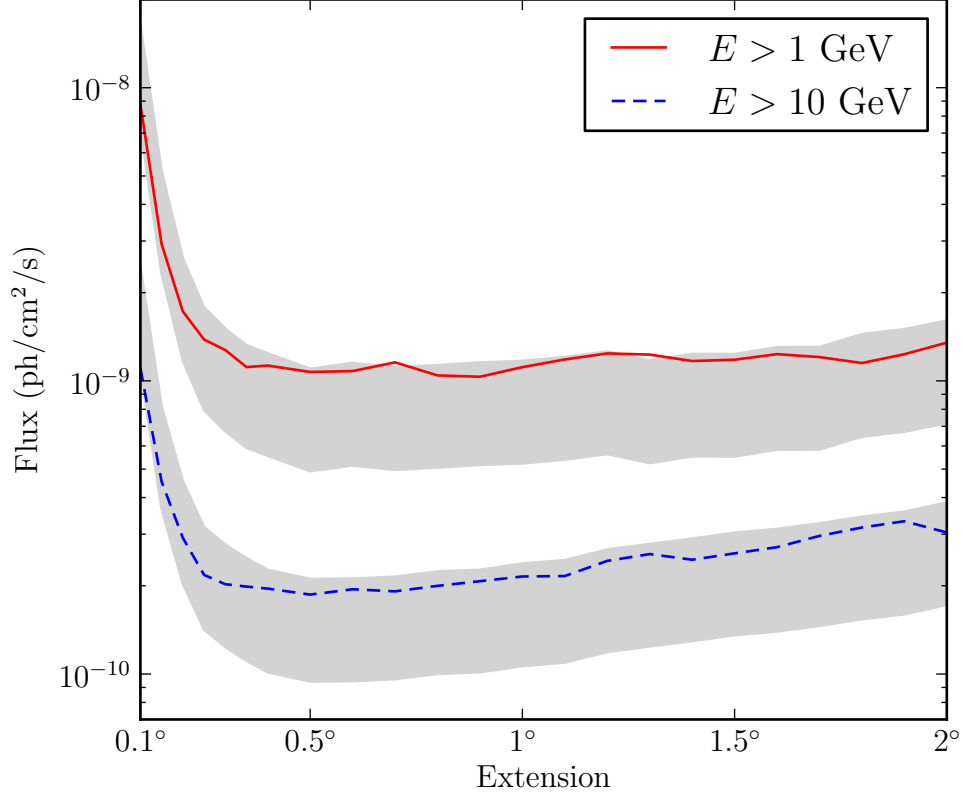
Fig. 6.— This plot shows our projected sensitiviy to extension after 10 years of operation for an assumed power-law source of spectral index 2 against a representative 10x the isotropic background in the energy range from 1-100 GeV (solid red) and 10-100 GeV (dashed blue). Flux is quoted in this energy range and the gray region is the projected sensitivity assuming that our sensitivity improves with $\sqrt{t}$ (top edge) and linearly with time (bottom edge). For small extended sources, our sensitivity to the extension of a source acutally improves better than $\sqrt{t}$ because at the highest energeries, where we are most sensitive to the extension of a source, the relevant background near the sources is in the Poisson instead of Gaussian regime. For large extended sources, the the relevant background is over a larger area and and our gain in sensitivity is closer to $\sqrt{t}$. This effect is even more pronounced for sources hard only above 10 GeV.
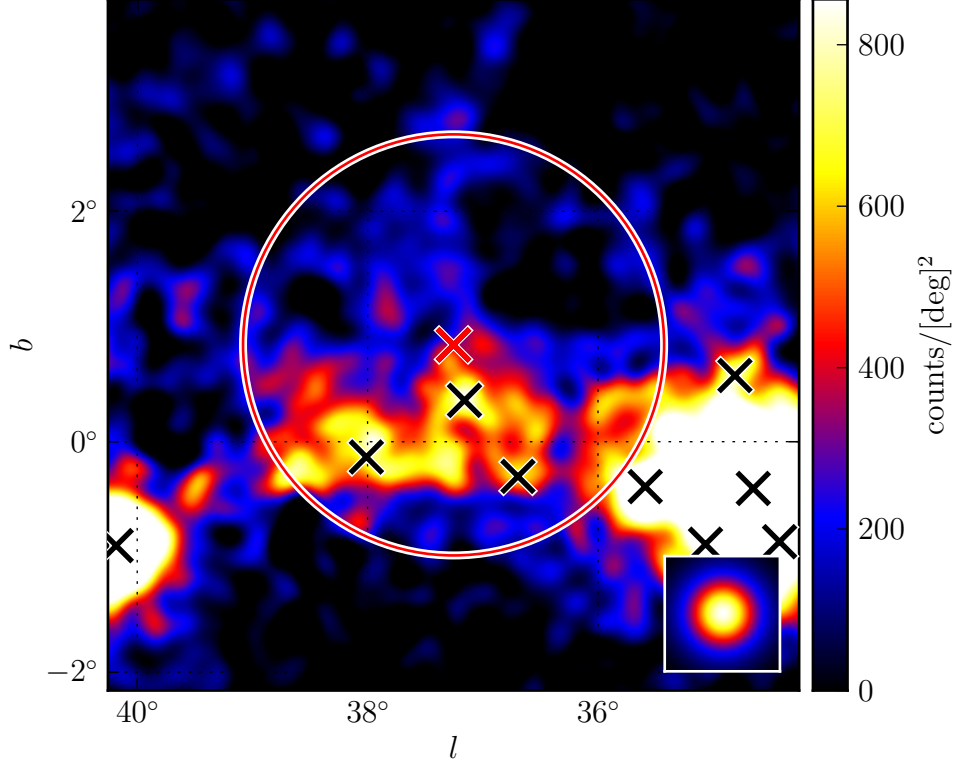
Fig. 7.— A Galactic and isotropic diffuse subtracted 1-100 GeV counts map of the region around 2FGL J1856.2+0450c smoothed by a 0.1° Gaussian kernel. The red cross and circle are the center and size of the best fit uniform disk spatial model. The result is statistically significant, but the extension encompasses many catalog sources and the emission does not look to be uniform. Instead, this source is probably fitting large-scale diffuse residual features. Although the fit is statistically significant, it is not physical and we manually discard candidates that appear like this.
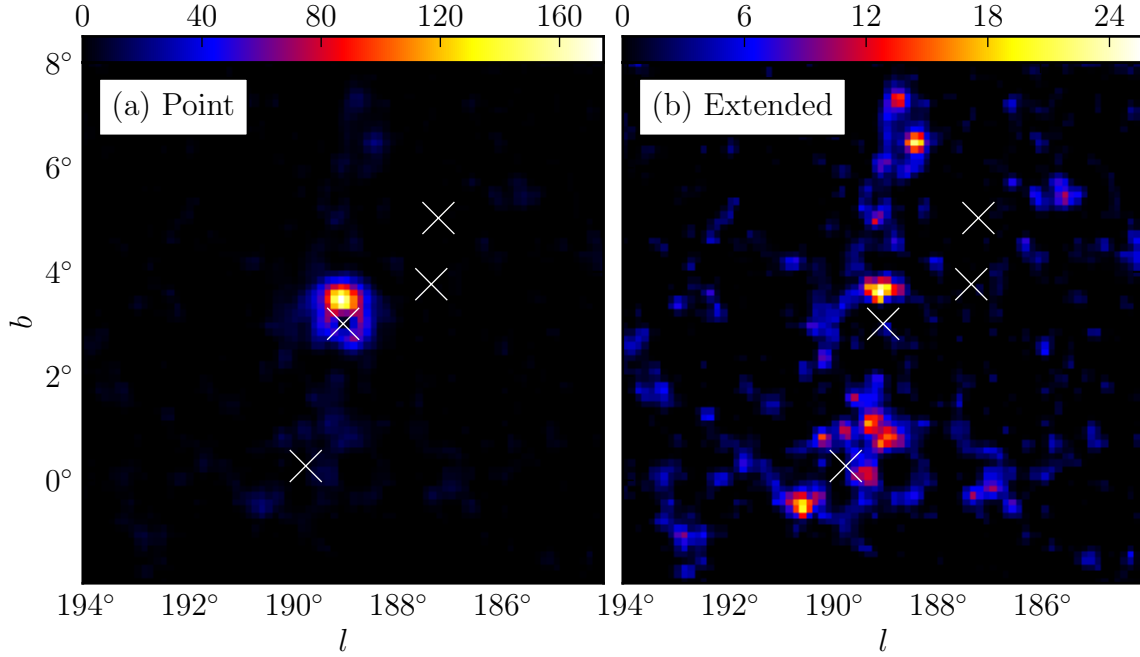
Fig. 8.— An example residual test statistic map generated for the supernova remnant IC443 using 1-100 GeV photons. Plot (a) is the residual TS fitting IC443 as a point source and plot (b) is the residual TS fitting IC443 as an extended source. The crosses in the plot represent all of the sources modeled in the region. Since there is residual TS greater than 160 fitting with the point hypothesis so it is not a good model of the source. On the other hand, the residual fitting IC443 as an extended source is much lower because IC443 is better fit by an extended source. These plots were generated for all extended source candidates to help validate the analysis.

Name	GLON	GLAT	σ	TS	TS$_{ext}$	Pos Err	Flux	Index
					$E > 1$GeV			
SMC	302.68°	-44.81°	1.75° ± 0.07° ± 0.02°	94.8	67.4	0.12°	3.3 ± 0.4	2.41 ± 0.17
LMC	279.10°	-32.61°	1.74° ± 0.05° ± 0.13°	1101.3	860.5	0.05°	15.5 ± 0.6	2.48 ± 0.06
IC443	189.05°	3.04°	0.36° ± 0.01° ± 0.04°	10719.8	510.4	0.01°	64.8 ± 1.2	2.23 ± 0.02
Vela X	263.34°	-3.11°	0.88°					
Centarus A	309.52°	19.42°	∼ 10°					
W28	6.50°	-0.27°	0.43° ± 0.02° ± 0.03°	1324.8	177.4	0.01°	58.0 ± 1.8	2.63 ± 0.03
W30	8.61°	-0.20°	0.36° ± 0.02° ± 0.02°	465.4	73.3	0.02°	30.7 ± 1.6	2.59 ± 0.04
W44	34.69°	-0.38°	0.36° ± 0.01° ± 0.02°	1903.3	217.7	0.01°	73.6 ± 1.8	2.68 ± 0.02
W51C	49.13°	-0.45°	0.28° ± 0.02° ± 0.05°	1819.5	115.7	0.01°	39.3 ± 1.3	2.35 ± 0.03
Cygnus Loop	74.22°	-8.46°	1.72° ± 0.05° ± 0.07°	356.5	356.5	0.06°	11.1 ± 0.7	2.53 ± 0.11
					$E > 10$GeV			
MSH 15-52	320.38°	-1.22°	0.20° ± 0.04° ± 0.03°	76.2	6.5	0.03°	0.6 ± 0.7	2.27 ± 0.73
HESS J1825-137	17.56°	-0.46°	0.65° ± 0.03° ± 0.01°	83.6	55.9	0.05°	1.8 ± 0.2	1.74 ± 0.19

Table 2: The twelve extended sources included in 2FGL. The top list are the extended sources analyzed using 1-100 GeV photons. The lower table are the sources analyzed using 10-100 GeV photons. The quoted flux is in units of 10^{-9}ph/cm^2/s and is the flux in the fit energy range (either 1-100 GeV or 10-100 GeV). All sources were fit using a uniform disk spatial template. The localization and extension were found using *pointlike* while the TS and spectral values were calculated using *gtlike*. TS and TS$_{ext}$ was computed with *gtlike* assuming the best fit uniform disk spatial model from *pointlike*. GLON and GLAT are Galactic longitude and latitude of the best fit extended source respectively. σ is the edge of the best fit uniform disk spatial model. The first error on σ is statistical and the second error is systematic (see section 5.2). Pos Err is the error on the localization of the source. Statistical errors are at the 1σ level. The Vela X and the Centarus A Lobes were not fit by our anaysis but are include for completeness (The Fermi LAT Collaboration & Timing Consortium (2010); Abdo et al. (2010c)). More information about these sources is in section 6.
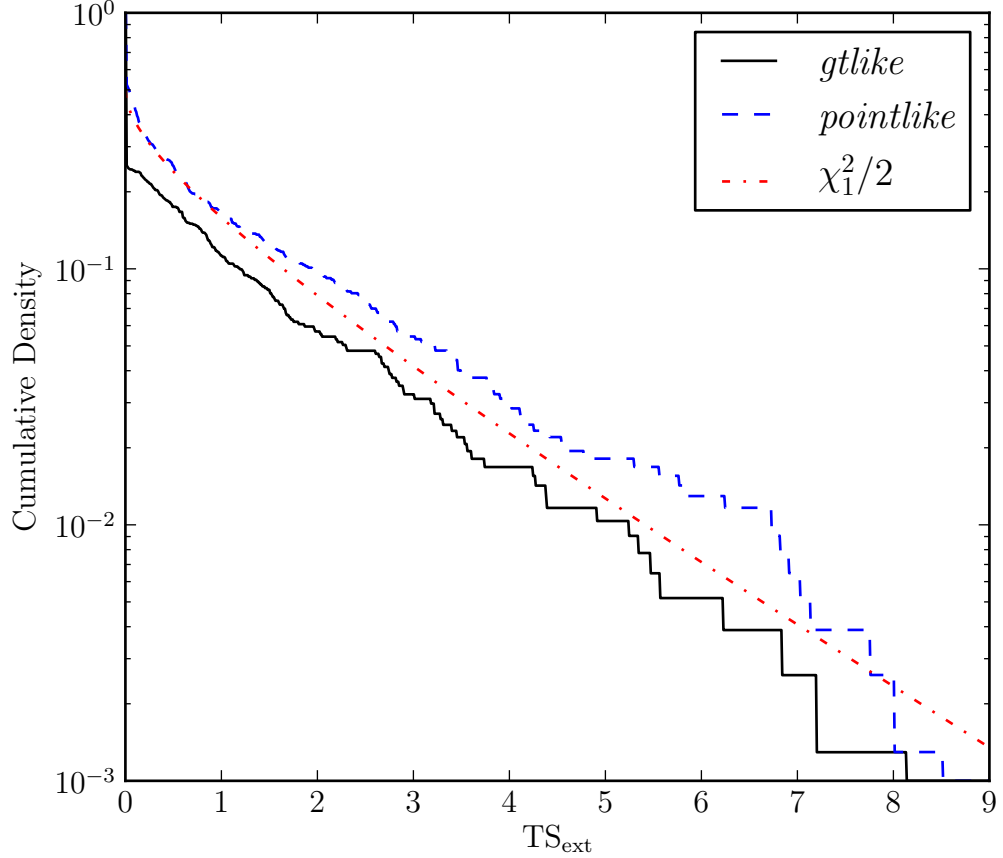
Fig. 9.— The cumulative density of TS_{ext} for 775 of the clean AGN in 2LAC which are significant above 1 GeV. AGN are expected to be unresolvable so overlaid on this plot is a $\chi^2/2$ distribution suggested by Wilks' theorem (see section 3.1). The TS_{ext} distribution computed with *pointlike* agrees with Wilks' theorem and confirms that we can use TS_{ext} as a test of extension. The distribution computed by *gtlike* is biased towards smaller values of TS_{ext}. This is because TS_{ext} is optimized using *pointlike* and minor difference in the *pointlike* and *gtlike* likelihood function will cause the best fit model to be slightly different. Because *gtlike*'s curve lies to the left of the theoretical distribution, this makes our test conservative. More information about this analysis is presented in section 7.

Name	GLON	GLAT	σ	TS	TS$_{\text{ext}}$	Pos Err	Flux	Index	Counterpart
					$E > 1$GeV				
2FGL J0823.0-4246	260.32°	-3.28°	0.37°±0.03°±0.02°	320.9	46.3	0.02°	8.5±0.7	2.20±0.09	Puppis A
2FGL J1627.0-2425c	353.08°	16.78°	0.41°±0.05°±0.02°	144.5	31.1	0.04°	6.5±0.6	2.49±0.14	Ophiuchus
2FGL J1712.4-3941	347.25°	-0.54°	0.56°±0.04°±0.01°	75.0	39.6	0.05°	4.2±0.9	1.47±0.12	RX J1713.7-3946
					$E > 10$GeV				
2FGL J0851.7-4635	266.29°	-1.43°	1.13°±0.08°±0.05°	116.1	87.2	0.07°	1.3±0.2	1.76±0.21	Vela Jr.
2FGL J1615.0-5051	332.38°	-0.14°	0.33°±0.04°±0.01°	53.4	16.3	0.04°	1.1±0.2	2.24±0.28	HESS J1616-508
2FGL J1615.2-5138	331.66°	-0.66°	0.42°±0.03°±0.01°	76.6	48.0	0.05°	1.2±0.2	1.77±0.24	HESS J1614-518
2FGL J1632.4-4753c	336.41°	0.22°	0.44°±0.04°±0.03°	127.8	64.5	0.04°	1.9±0.2	2.29±0.21	HESS J1632-478
2FGL J1837.3-0700c	25.08°	0.13°	0.35°±0.08°±0.03°	46.2	18.8	0.07°	1.0±0.2	1.63±0.29	HESS J1837-069
2FGL J2021.5+4026	78.18°	2.19°	0.59°±0.03°±0.02°	222.2	116.4	0.04°	1.8±0.2	2.31±0.19	Gamma Cygni

Table 3: The 8 new source candidates found by the extended source search. Three new extended sources were found using photons with energies above 1 GeV and five new candidates were found using photons with energies above 10 GeV. The columns in this table have the same meaning as in table 2. More information about these sources can be found in section 8.

Name	TS_{inc}	TS_{ext}	$GLON_1$	$GLAT_1$	$Flux_1$	$Index_1$	$GLON_2$	$GLAT_2$	$Flux_2$	$Index_2$
					$E > 1\,GeV$					
2FGLJ0823.0-4246	22.1	46.3	260.59°	-3.27°	2.1 ± 0.6	2.0 ± 0.2	260.24°	-3.20°	5.4 ± 0.7	2.4 ± 0.2
2FGLJ1627.0-2425c	20.0	31.1	353.01°	16.98°	3.1 ± 0.6	2.6 ± 0.3	353.24°	16.66°	2.5 ± 0.6	2.5 ± 0.4
2FGLJ1712.4-3941	6.4	39.6	347.28°	-0.07°	0.2 ± 0.1	0.6 ± 0.5	347.22°	-0.27°	2.4 ± 0.7	1.9 ± 0.2
					$E > 10\,GeV$					
2FGLJ0851.7-4635	16.1	87.2	266.79°	-1.32°	0.2 ± 0.1	1.8 ± 0.5	266.41°	-1.39°	0.2 ± 0.1	1.5 ± 0.6
2FGLJ1615.0-5051	11.9	16.3	332.39°	-0.08°	0.4 ± 0.1	2.3 ± 0.6	332.43°	-0.36°	0.4 ± 0.1	2.3 ± 0.5
2FGLJ1615.2-5138	37.0	48.0	331.76°	-0.37°	0.4 ± 0.1	1.3 ± 0.5	331.47°	-0.80°	0.4 ± 0.1	2.0 ± 0.4
2FGLJ1632.4-4753c	40.6	64.5	336.52°	0.17°	0.7 ± 0.2	2.8 ± 0.5	336.13°	0.37°	0.5 ± 0.1	1.7 ± 0.4
2FGLJ1837.3-0700c	12.6	18.8	25.04°	0.26°	0.3 ± 0.1	1.2 ± 0.5	25.10°	-0.05°	0.4 ± 0.1	2.0 ± 0.5
2FGLJ2021.5+4026	24.3	116.4	78.28°	1.95°	0.3 ± 0.1	5.0 ± 0.0	78.15°	2.20°	0.6 ± 0.1	1.7 ± 0.4

Table 4: For the new extended source candidates in table 3, we describe the results of the dual localization procedure described in section 2.4. Here, the extended source candidate is not fit as an extended source but instead fit as two point sources. The dual localization is performed with *pointlike* and results in the best fit position of the two sources ($GLON_1$, $GLAT_1$) and ($GLON_2$, $GLAT_2$). The change in likelihood and spectral values are then computed using *gtlike* with the best fit positions found by *pointlike*. TS_{inc} is the increase in TS fitting the region as two sources compared to fitting a single point source and is computed using *gtlike* with the best fit positions taken from table 3. For all of our candidates, $TS_{ext} > TS_{inc}$ which shows that an extended source fits the source better than two point sources. As in table 2, flux is measured in units of 10^{-9}ph/cm^2/s and is either the 1-100 GeV or 10-100 GeV photon flux.

– 41 –

Name	$\mathrm{TS}_{pointlike}$	TS_{gtlike}	$\mathrm{TS}_{\mathrm{alt,diff}}$	$\mathrm{TS}_{\mathrm{ext}\,pointlike}$	$\mathrm{TS}_{\mathrm{ext}\,gtlike}$	$\mathrm{TS}_{\mathrm{ext\,alt,diff}}$	σ	$\sigma_{\mathrm{alt,diff}}$	$\sigma_{\mathrm{alt,psf}}$
				$E > 1\mathrm{GeV}$					
2FGL J0823.0-4246	350.9	320.9	352.5	66.0	46.3	53.6	0.37°	0.39°	0.38°
2FGL J1627.0-2425c	170.2	144.5	112.6	43.9	31.1	23.9	0.41°	0.40°	0.39°
2FGL J1712.4-3941	80.9	75.0	43.4	47.4	39.6	22.2	0.56°	0.56°	0.54°
				$E > 10\mathrm{GeV}$					
2FGL J0851.7-4635	116.7	116.1	122.3	87.1	87.2	90.4	1.13°	1.16°	1.17°
2FGL J1615.0-5051	52.4	53.4	55.6	17.5	16.3	17.4	0.33°	0.32°	0.32°
2FGL J1615.2-5138	76.3	76.6	86.3	44.0	48.0	52.6	0.42°	0.43°	0.43°
2FGL J1632.4-4753c	126.6	127.8	120.7	63.9	64.5	64.1	0.44°	0.44°	0.47°
2FGL J1837.3-0700c	45.4	46.2	39.0	18.5	18.8	16.6	0.35°	0.34°	0.38°
2FGL J2021.5+4026	234.3	222.2	235.6	135.9	116.4	121.4	0.59°	0.60°	0.60°

Table 5: For the new extended sources, this table shows the results of fitting the new extended sources with an alternate diffuse model and an alternate PSF (see section 5.2). It also compares the best fit results of *pointlike* to *gtlike*. $\mathrm{TS}_{pointlike}$ and TS_{gtlike}, and $\mathrm{TS}_{\mathrm{alt,diff}}$ are the TS from *pointlike*, *gtlike*, and *gtlike* with the alternate diffuse model respectively. $\mathrm{TS}_{\mathrm{ext}\,pointlike}$, $\mathrm{TS}_{\mathrm{ext}\,gtlike}$, and $\mathrm{TS}_{\mathrm{ext\,alt,diff}}$ are the $\mathrm{TS}_{\mathrm{ext}}$ from *pointlike*, *gtlike*, and *gtlike* with the alternate diffuse model respectively. σ is the best fit extension using *pointlike* and the standard PSF and diffuse model. $\sigma_{\mathrm{alt,diff}}$ is the best fit extension using the alternate diffuse model and $\sigma_{\mathrm{alt,psf}}$ is the best fit extension using the alternate PSF. The difference between these extensions is used to compute the systematic error on extension in table 2 and table 3.
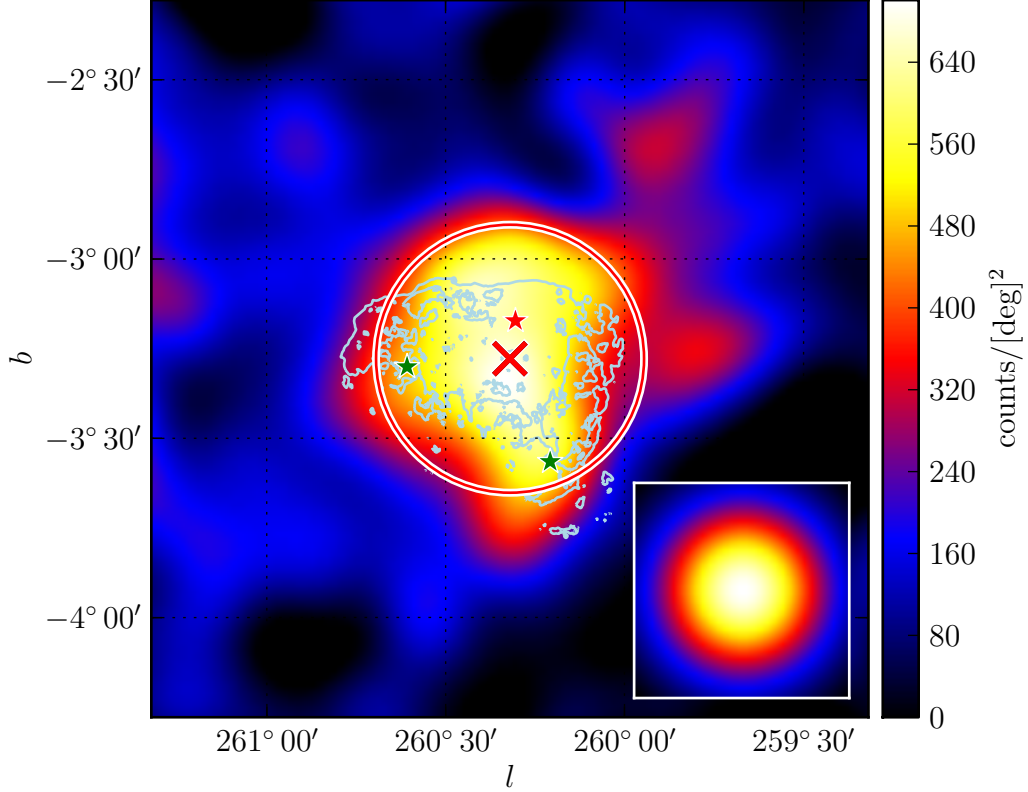
Fig. 10.— A Galactic and isotropic diffuse subtracted 1-100 GeV counts map of the region around 2FGL J0823.0-4246 smoothed by a 0.1° Gaussian kernel. The red star is the catalog position of this source. The red cross and circle are the best fit position and extension of this source assuming a uniform disk spatial model. The two green stars are the positions of the sources 2FGL J0823.4-4305 and 2FGL J0821.0-4254 which were removed because they are part of the extended source. This source is spatially coincident with the Puppis A SNR. The light blue contours are an X-ray image of Puppis A observed by ROSAT (Petre et al. (1996)). There is good spatial overlap between the LAT and X-ray emission. Even though the Vela pulsar is over 3 degrees away from the source, because it is so bright it can be seen on the top left. More information about this source can be found in section 8.1.
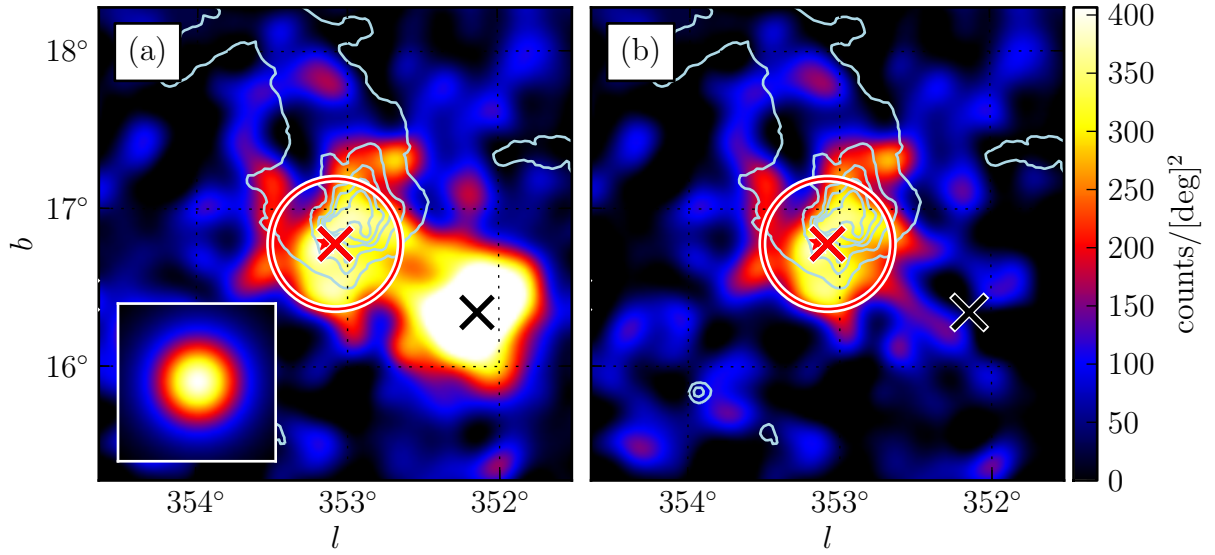
Fig. 11.— A Galactic and isotropic diffuse subtracted 1-100 GeV counts map of the region around 2FGL J1627.0-2425 smoothed by a 0.1° Gaussian kernel. Plot (a) has the diffuse emission model subtracted and plot (b) has the diffuse emission and the background source 2FGL J1625.7-2526. subtracted. The red star is the catalog's position of this source. The red cross and circle are the best position and extension of this source assuming a uniform disk spatial model. The light blue contours are from a 100 micrometer infrared image of the region as seen by IRAS (Young et al. (1986)). This source is in the Ophiuchus region and most likely represents unmodeled diffuse emission. More information about this source can be found in section 8.2.
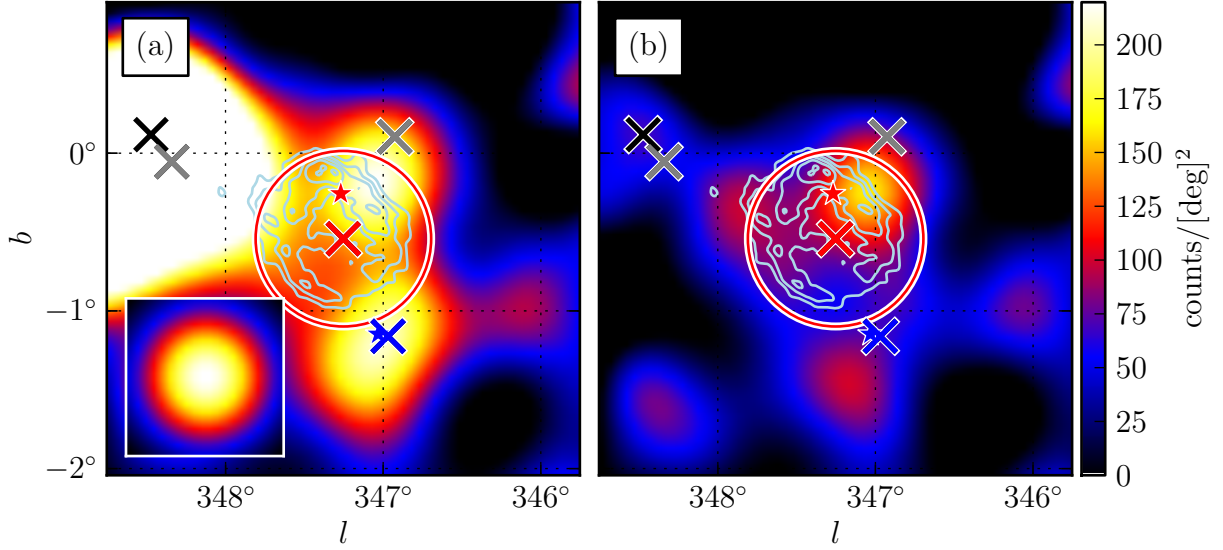
Fig. 12.— A Galactic and isotropic diffuse subtracted 1-100 GeV counts map of the region around 2FGL J1712.4-3941 smoothed by a 0.25° Gaussian kernel. Plot (a) has the diffuse emission model subtracted and plot (b) has the diffuse emission and all background sources subtracted. This source is spatially coincident with RX J1713.7-3946 was was recently reported by (Abdo et al. (2011c)). The light blue contours are from the TeV image observed by H.E.S.S. (Aharonian et al. (2007b)). The region was analyzed with the same background model as (Abdo et al. (2011c)). Source A (blue cross) is spatially coincident with 2FGL J1715.4-4024c (blue star). The gray crosses represent from left to right the position of source B and C which were added to the background model. More information about this source can be found in section 8.3.
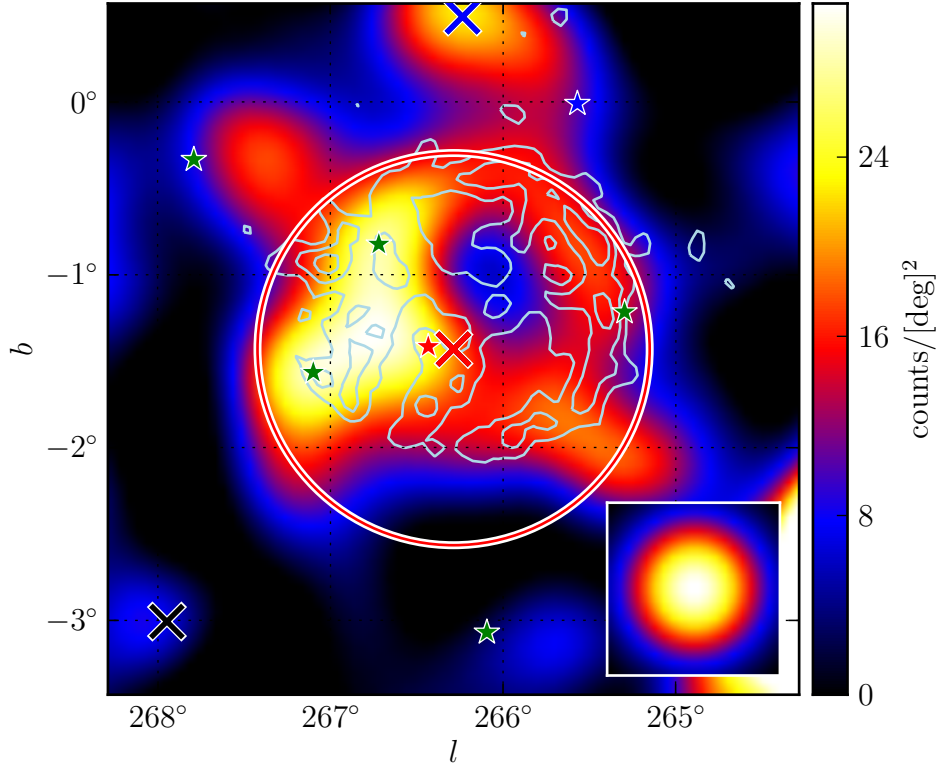
Fig. 13.— A Galactic and isotropic diffuse subtracted 10-100 GeV counts map of the region around 2FGL J0851.7-4635 smoothed by a 0.25° Gaussian kernel. This image is smoothed by a larger kernel because it is significantly larger than the other sources. The red star is the catalog position of this source. The red cross and circle are the best fit position and extension of the source assuming a uniform disk spatial model. The inner three green stars are (from left to right) 2FGL J0853.5-4711, 2FGL J0855.4-4625, and 2FGL J0848.5-4535 which were removed because they are part of the extended source. The farther away green stars are (from left to right) 2FGL J0901.7-4655 and 2FGL J0858.0-4815 which were removed because they were not significant above 10 GeV. The blue cross is the relocalized position of 2FGL J0854.7-4501. This extended source is spatially coincident with the Vela Jr SNR. The light blue contours are from the TeV image of Vela Jr. observed by H.E.S.S (Aharonian et al. (2007a)). More information about this source can be found in section 8.4.
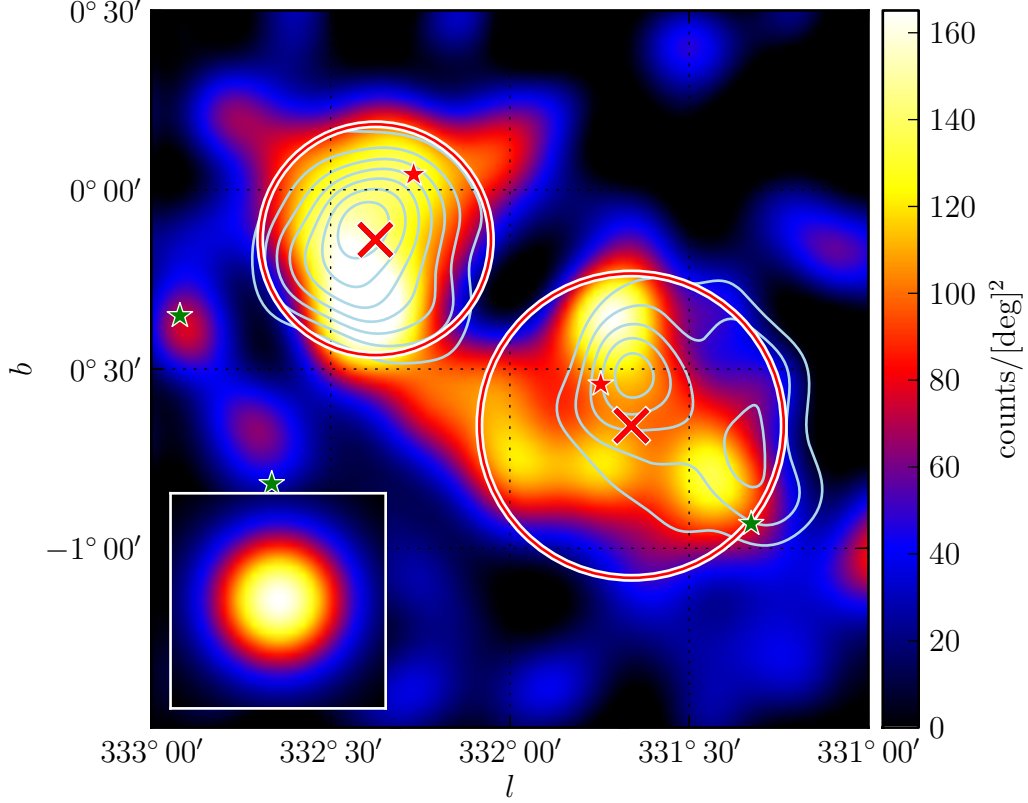
Fig. 14.— A Galactic and isotropic diffuse subtracted 10-100 GeV counts map of the region around 2FGL J1615.0-5051 (upper left) and 2FGL J1615.2-5138 (lower right) smoothed by a 0.1° Gaussian kernel. The red stars are the catalog positions of these sources. The red stars and circles are the best fit positions and extensions of these sources assuming uniform disk spatial models. The green star inside the extension of 2FGL J1615.2-5138 is 2FGL J1614.9-5212 which was removed because it is part of the extended source. The green stars to the left are 2FGL J1619.7-5040c and 2FGL J1620.6-5111c which were removed because they were not significant above 10GeV. These are shown as green stars. The light blue contours are from the TeV image of the extended sources HESS J1616-508 (left) and the extended source HESS J1614-518 (right) observed by H.E.S.S (Aharonian et al. (2006)) 2FGL J1615.0-5051 is spatially consistent with HESS J1616-508 and 2FGL J1615.2-5138 is spatially consistent with HESS J1614-518. Figure 18 (a) and (b) shows the GeV and TeV SEDs for these sources. More information about 2FGL J1615.0-5051 can be found in section 8.5 and 2FGL J1615.2-5138 in section 8.6.
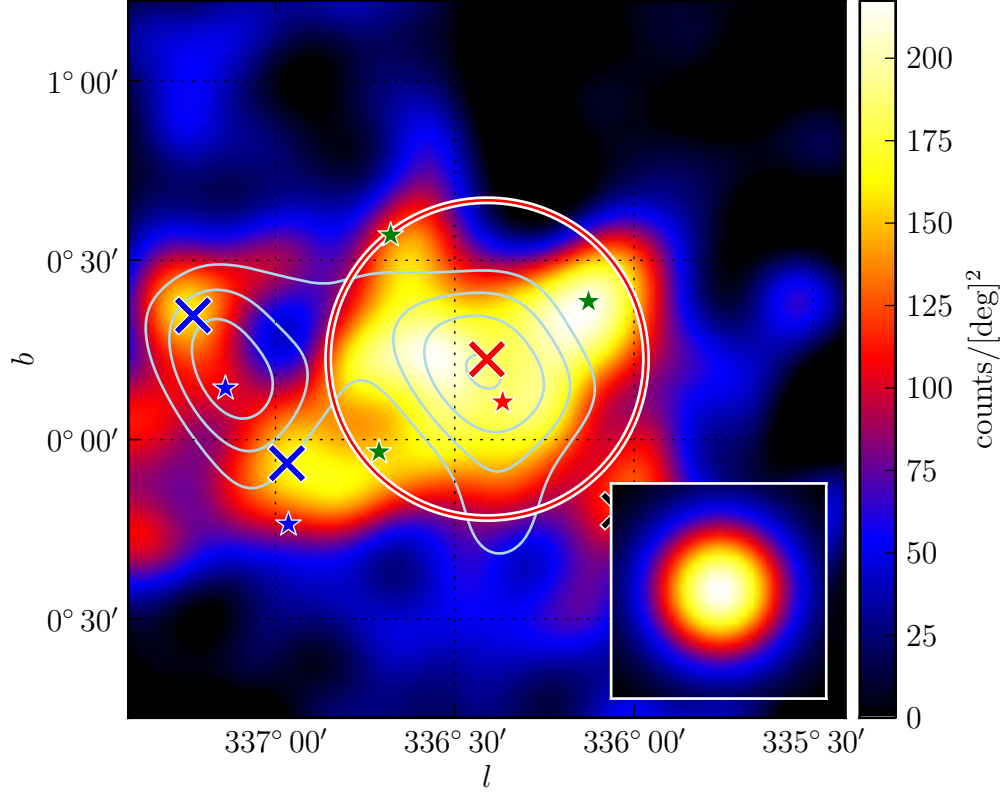
Fig. 15.— A Galactic and isotropic diffuse subtracted 10-100 GeV counts map of the region around 2FGL J1632.4-4753c smoothed by a 0.1° Gaussian kernel. This source is in a crowded region. The red star is the catalog position of this source. The red cross and circle are the best fit position and extension 2FGL J1632.4-4753c assuming a uniform disk spatial model. The three green crosses inside the extension are 2FGL J1631.7-4720c, 2FGL J1630.2-4752, and 2FGL J1634.4-4743c.4-4820c which were removed because they are part of the extended source. The blue stars and crosses are the catalog positions and the relocalized positions of (from left to right) 2FGL J1635.4-4717c and 2FGL J1636.3-4740c. The farther away green stars are other catalog sources which were removed because they are not significant above 10 GeV. This extended source is spatially coincident with the extended H.E.S.S source HESS J1632-478. The light blue contours are from the TeV image observed by H.E.S.S. (Aharonian et al. (2006)). Figure 18 (c) shows the GeV and TeV SED for this source. More information about this source can be found in section 8.7.
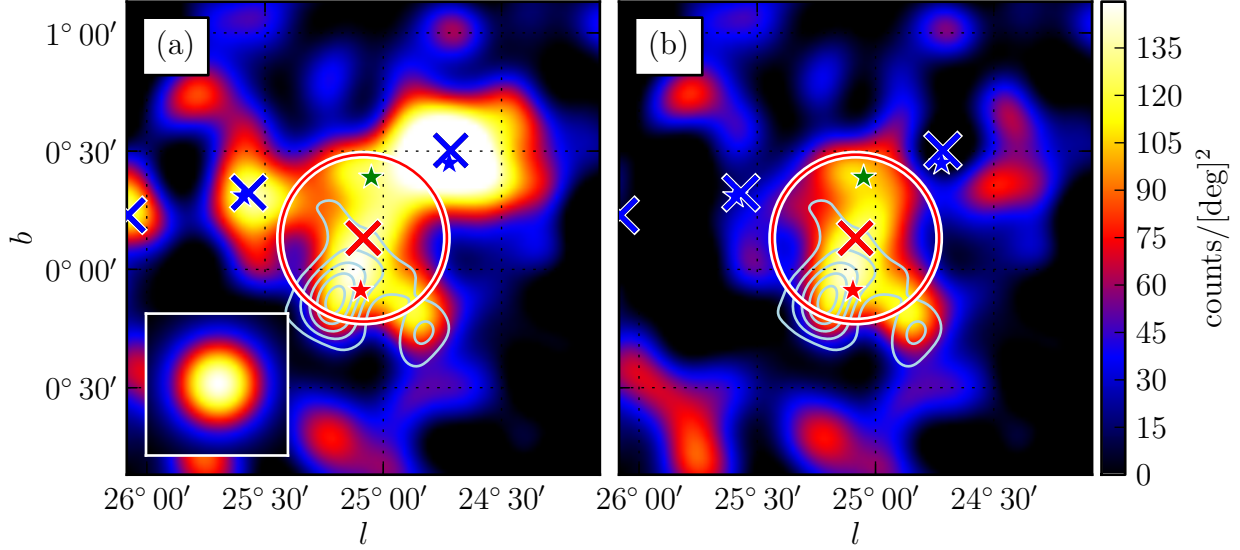
Fig. 16.— A Galactic and isotropic diffuse subtracted 10-100 GeV counts map of the region around 2FGL J1837.3-0700c smoothed by a 0.1° Gaussian kernel. Plot (a) has the diffuse emission model subtracted and plot (b) has the diffuse emission and all background sources subtracted. The red star is the catalog position of this source. The red cross and circle are the best fit position and extension of 2FGL J1837.3-0700c assuming a uniform disk spatial model. The blue stars and crosses are the catalog position and the relocalized position of (from left to right) 2FGL J1839.3-0558c, 2FGL J1836.8-0623c, and 2FGL J1834.7-0705c. The green cross inside the extension is 2FGL J1835.5-0649 which was removed because it is part of the extended source. The farther away green star is 2FGL J1839.0-0539 which was removed because it is not significant above 10 GeV. This source is spatially coincident with the TeV source HESS J1837-069. The light blue contours are from the TeV image observed by H.E.S.S. (Aharonian et al. (2006)). Figure 18 (d) shows the GeV and TeV SED for this source. More information about this source can be found in section 8.8.
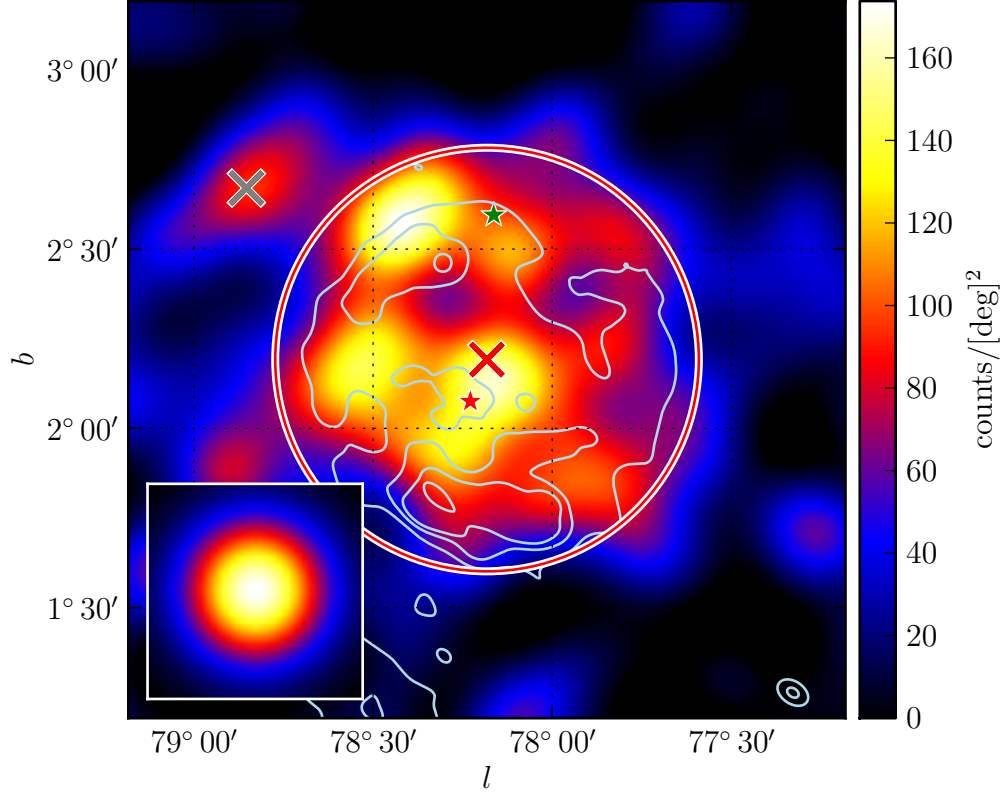
Fig. 17.— A Galactic and isotropic diffuse subtracted 10-100 GeV counts map of the region around 2FGL J2021.5+4026 smoothed by a 0.1° Gaussian kernel. The red star is the catalog position of 2FGL J2021.5+4026. The red cross and circle are the best fit position and extension 2FGL J2021.5+4026 assuming a uniform disk spatial model. The green cross inside the extension is 2FGL J2019.1+4040 which was removed because it is part of the extended source. The farther away green stars represent other catalog sources which were removed because they were not significant above 10 GeV. The gray cross is the position a source not in the two year catalog which was added to the region. 2FGL J2021.5+4026 is spatially coincident with the Gamma Cygni SNR. The light blue contours are from a 408MHz image of Gamma Cygni observed by the Canadian Galactic Plane Survey. More information about this source can be found in section 8.9.
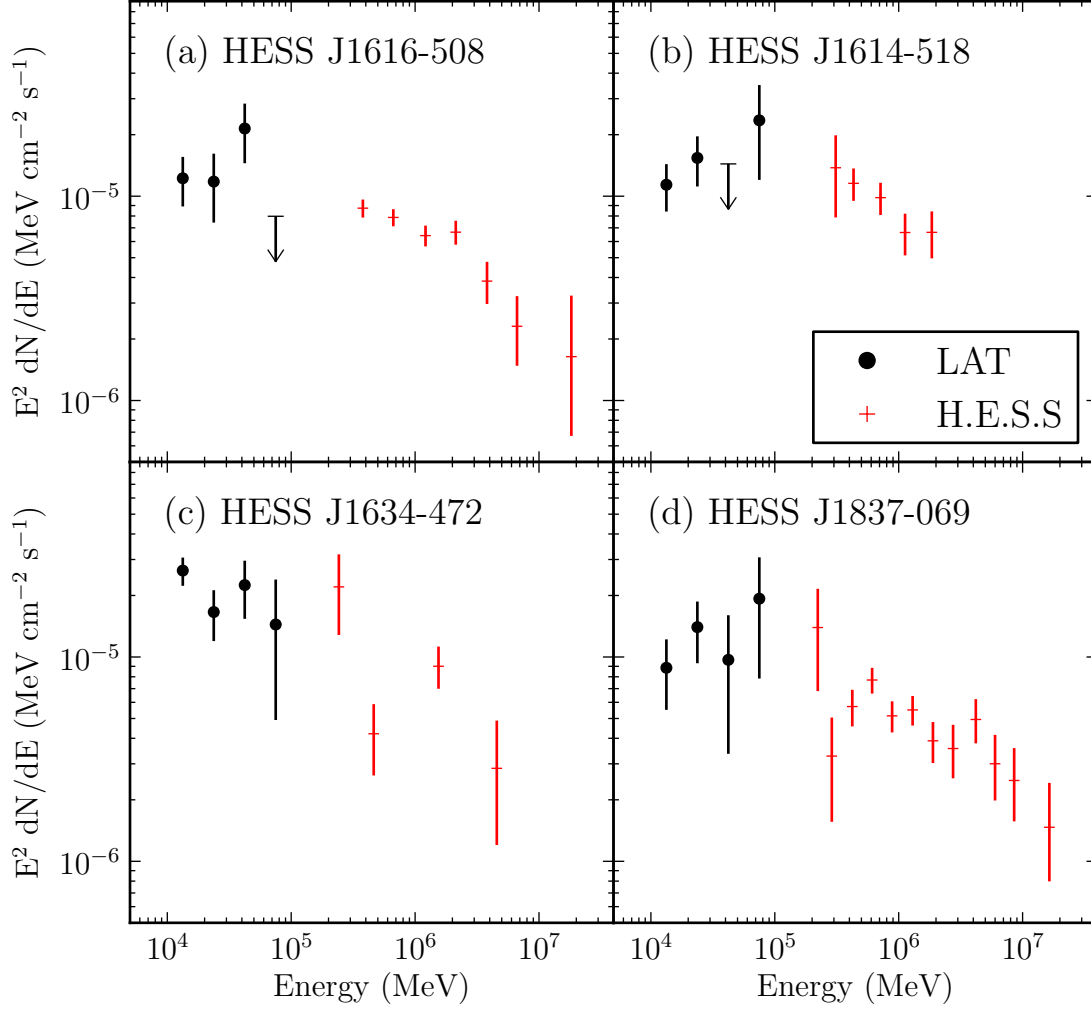
Fig. 18.— The spectral energy distribution of four the extended sources associated with extended TeV sources. The black points with circular markers are the LAT data points. The red points with dashed markers are H.E.S.S points of associated sources. Plot (a) shows the GeV SED of 2FGL J1615.0-5051 and the TeV SED of HESS J1616-508. Plot (b) shows 2FGL J1615.2-5138 and HESS J1614-518 Plot (c) shows 2FGL J1632.4-4753c and HESS J1632-478. Plot (d) shows 2FGL J1837.3-0700c and HESS J1837-069. The H.E.S.S. data points are from (Aharonian et al. (2006)) The LAT upper limits are at the 95% confidence level. Both LAT and H.E.S.S. spectral errors are systematic only.

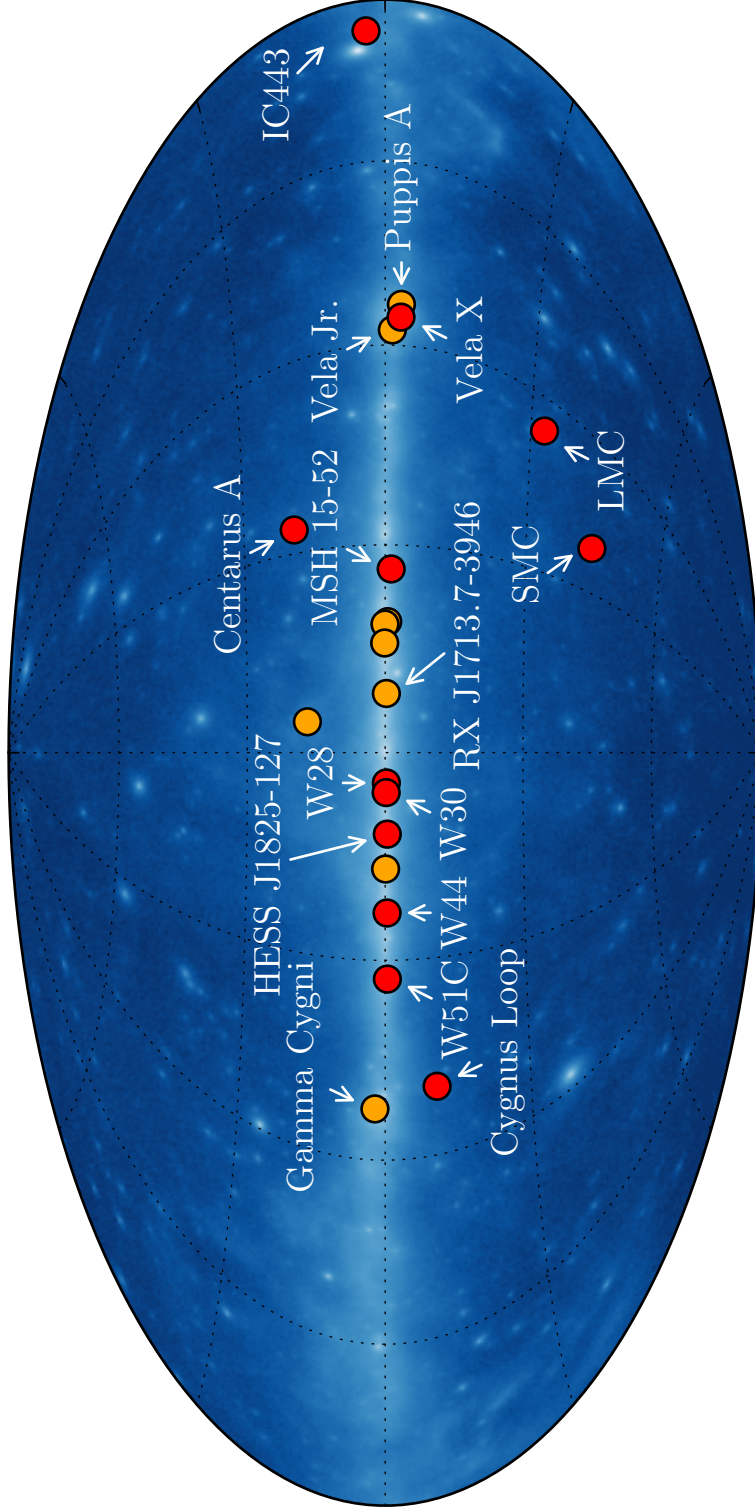Fig. 19.— A plot of all GeV extended sources detected by the LAT with two years of data. The twelve extended sources included in 2FGL are the red markers and the nine additional extended sources analyzed in this paper are the orange markers. The extended sources are overlaid on an Aitoff projection Galactic coordinate map of all 100 MeV to 100 GeV photons measured by the LAT in the two year time interval of this analysis.
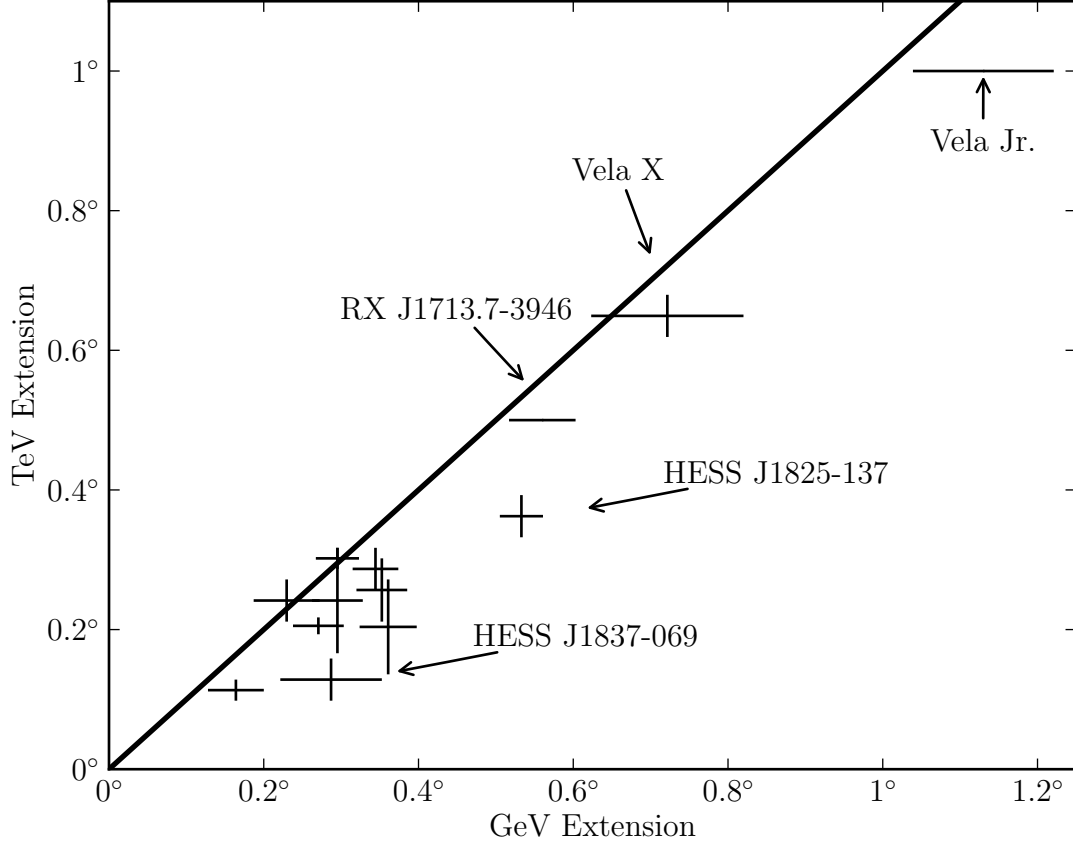
Fig. 20.— A comparison of the GeV and TeV sizes of LAT extended sources detected by TeV instruments. The TeV extensions of W30, 2FGL J1837.3-0700c, 2FGL J1632.4-4753c, 2FGL J1615.0-5051, and 2FGL J1615.2-5138 are from the H.E.S.S. Galactic plane survey (Aharonian et al. (2006)). The TeV extensions of MSH 15-52, HESS J1825-137, Vela X, Vela Jr., RX J1713.7-3946 and W28 are respectively from H.E.S.S. (Aharonian et al. (2005, 2006b,c, 2007a,b, 2008)). The TeV extension of IC443 is from Veritas (Acciari et al. (2009)) and W51c is from Magic (Julian Krause & on behalf of MAGIC (2011)). The LAT extension of Vela X is from (The Fermi LAT Collaboration & Timing Consortium (2010)). Except for RX J1713.7-3946 Vela Jr., the TeV sources were fit with a Gaussian spatial model so the plotted GeV and TeV extensions were first converted to r_{68} (see section 2.5). Because of their large size, the RX J1713.7-3946 and Vela Jr. were not directly fit in TeV. The TeV radius of RX J1713.7-3946 is taken to be $0.5°$ and Vela Jr. to be $1°$ and the LAT size is not converted to r_{68}. The LAT extension errors are the statistical and systematic errors added in quadrature. This plot shows that there is a correlation between the GeV and TeV sizes of sources. The TeV size of MSH 15-52, HESS J1614-518, HESS J1632-478, and HESS J1837-069 have only been reported with an elliptical Gaussian fit and so the plotted size is the average of semi-major and semi-minor axis.
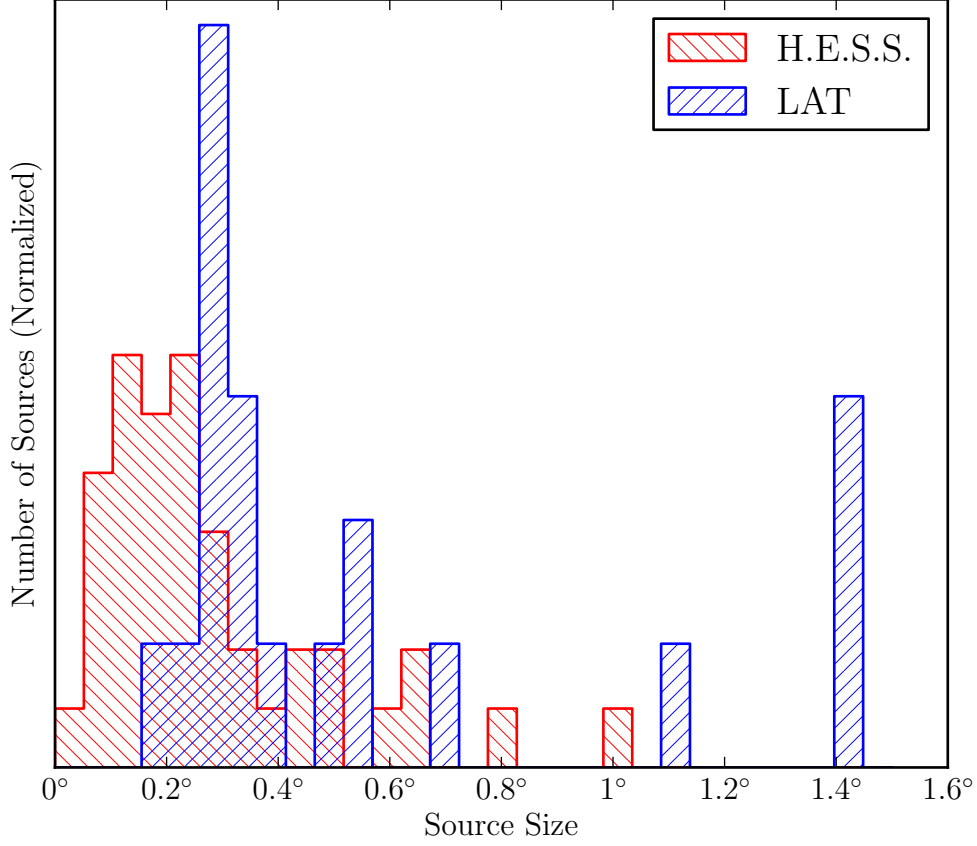
Fig. 21.— A comparison of the size of detected LAT and H.E.S.S sources. The extension of the 22 extended LAT sources comes from table 2, table 3, and the LAT extension of Vela X is taken from (The Fermi LAT Collaboration & Timing Consortium (2010)). The Centarus A lobes, which have an extension $10°$, are not included in the plot (Abdo et al. (2010c)). The TeV extension of the 42 extended H.E.S.S. sources comes from the H.E.S.S. Source CatalogThe H.E.S.S. Collaboration (2011). Except for RX J1713.7-3946 and Vela Jr., the H.E.S.S. sources were fit with a Gaussian spatial model and so the LAT and H.E.S.S. sizes are first converted to r_{68}. (see section 2.5). Because the spatial morphology of RX J1713.7-3946 and Vela Jr. is poorly matched by a Gaussian, the TeV sizes are assuming a uniform disk spatial model and so neither the GeV nor TeV sizes were converted. This plot shows that TeV experiments are sensitive to smaller extended sources.
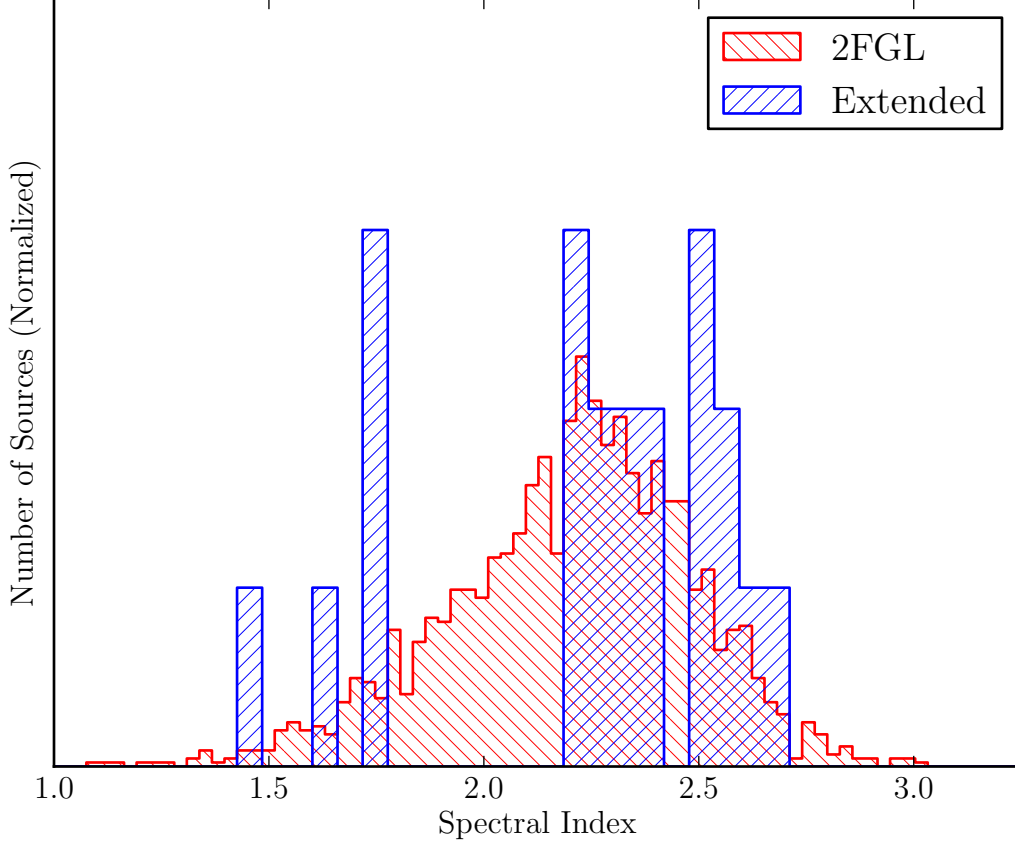
Fig. 22.— The distribution of spectral indices of all 1873 2FGL sources in red and all spatially extended sources in blue. in 2FGL. The spectral indices of LAT extended sources are taken from table 2 table 3. The index of Centarus A is taken to be 2.58 from the two year catalog (Abdo et al. (2011b)) and the index of Vela X is taken to be 2.41 from (The Fermi LAT Collaboration & Timing Consortium (2010)). This plot shows that many of the LAT extended sources have a hard (< 2) spectral index.

Appendices
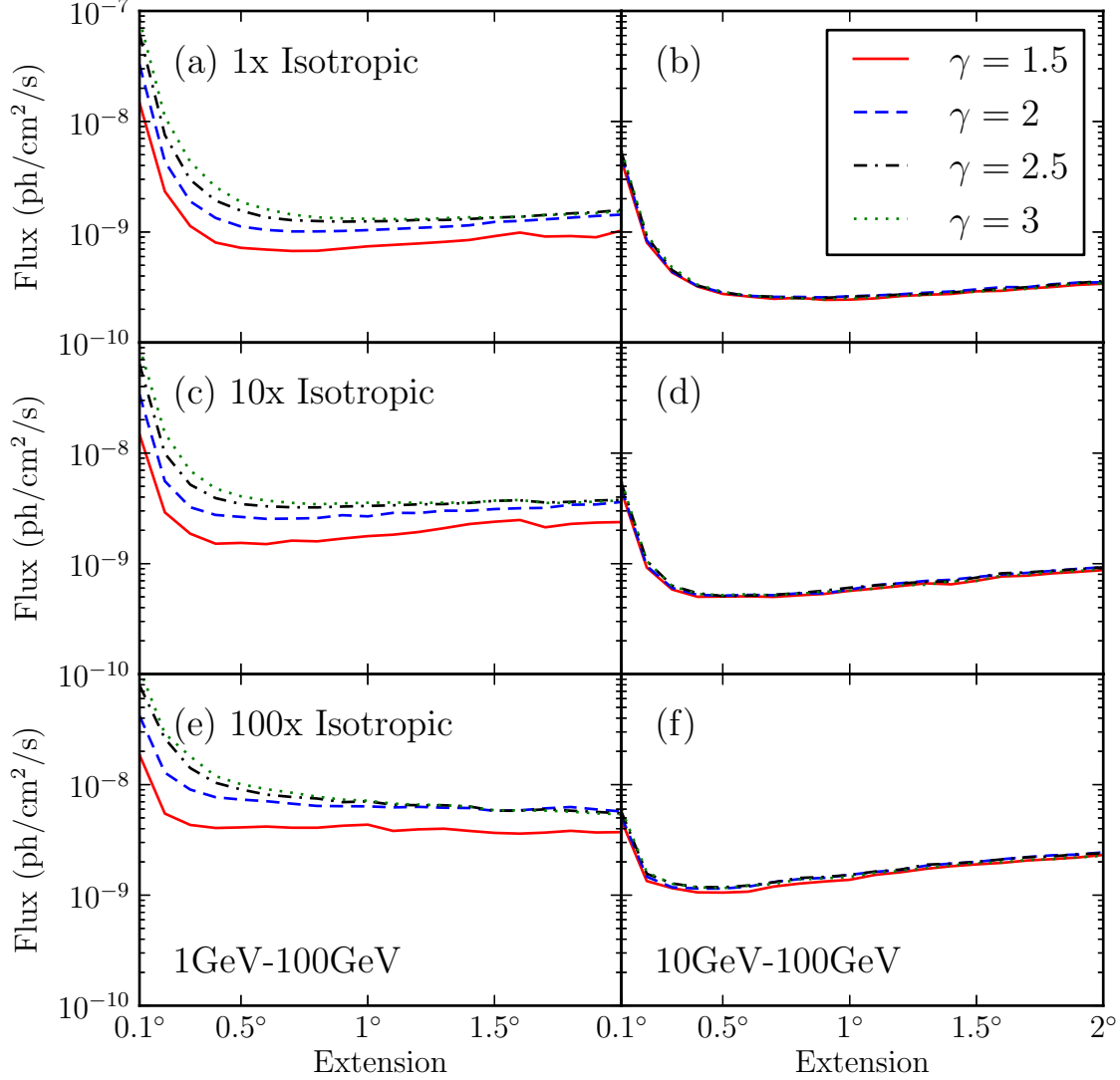
Fig. 23.— These six plots condense the LAT detection threshold for all four spectral indices shown in figure 4 (1.5, 2, 2.5, and 3) and all three background levels shown in 5. (1x, 10x, and 100x the Sreekumar-like isotropic spectrum). The plots have the same meaning as in figure 4 The left plots are the detection threshold when using 1-100 GeV photons and the right plots are the detection threshold when using 10-100 GeV photons. This plot shows that when using only high energy photons with an improved angular resolution, our detection threshold is only weakly a function of spectral index. The numeric values plotted here are tabulated in table 6. More information about this plot is presented in section 4.

1GeV < E < 100GeV

γ	BG	0.1°	0.2°	0.3°	0.4°	0.5°	0.6°	0.7°	0.8°	0.9°	1°	1.1°	1.2°	1.3°	1.4°	1.5°	1.6°	1.7°	1.8°	1.9°	2°
1.5	x1	148.3	23.2	11.2	8.0	7.1	6.9	6.8	6.8	7.0	7.3	7.5	7.7	8.0	8.3	9.1	9.8	9.0	9.1	8.8	10.2
	x10	146.9	29.0	18.5	15.1	15.4	15.0	14.7	15.6	16.6	17.3	18.0	19.1	20.7	22.5	23.6	24.3	21.2	22.8	23.3	23.6
	x100	184.3	55.1	43.0	41.0	40.7	41.7	40.3	40.8	43.0	43.6	38.3	39.5	40.1	38.5	36.5	35.8	36.5	38.1	36.6	37.1
2	x1	327.5	43.1	18.7	13.3	11.2	10.4	10.1	10.1	10.2	10.4	10.6	10.9	11.1	11.5	12.3	12.6	13.0	13.4	13.8	14.2
	x10	336.1	55.3	32.2	27.4	26.3	25.3	25.5	25.8	27.2	26.6	27.6	28.5	30.1	29.9	30.8	31.8	31.9	34.2	34.2	36.1
	x100	409.6	128.1	88.6	76.2	72.7	71.4	67.8	65.2	63.6	63.7	62.0	63.1	62.4	61.1	56.0	58.4	60.1	62.1	59.5	55.9
2.5	x1	622.9	75.0	29.6	19.0	15.5	13.6	12.8	12.7	12.4	12.5	12.6	12.9	12.8	13.1	13.4	13.7	14.1	14.6	15.0	15.7
	x10	641.5	98.2	51.8	39.2	34.7	33.1	32.6	32.3	33.0	33.4	33.8	34.5	34.5	35.4	37.0	37.2	35.6	36.2	37.1	37.8
	x100	789.7	260.3	136.9	102.7	90.1	80.8	77.2	74.9	69.1	70.8	65.8	64.5	64.3	62.3	57.1	57.1	58.8	57.3	55.6	54.2
3	x1	842.0	109.6	42.9	25.4	18.7	15.9	14.3	13.5	13.3	13.2	13.1	13.1	13.4	13.5	13.5	13.6	14.1	14.3	14.7	15.3
	x10	919.0	153.8	69.7	48.1	40.9	37.6	35.7	34.9	35.3	35.3	35.3	35.2	35.1	35.5	37.0	37.7	35.3	35.5	36.4	37.5
	x100	1077.5	289.1	180.2	119.2	101.0	92.4	86.2	79.3	74.3	70.8	67.2	66.4	65.0	62.9	58.4	56.6	57.4	55.9	54.3	52.2

10GeV < E < 100GeV

γ	BG	0.1°	0.2°	0.3°	0.4°	0.5°	0.6°	0.7°	0.8°	0.9°	1°	1.1°	1.2°	1.3°	1.4°	1.5°	1.6°	1.7°	1.8°	1.9°	2°
1.5	x1	44.4	8.1	4.3	3.2	2.7	2.6	2.5	2.5	2.4	2.4	2.5	2.6	2.7	2.7	2.9	2.9	3.1	3.2	3.3	3.4
	x10	45.2	9.3	5.9	5.0	4.9	5.1	5.0	5.2	5.3	5.7	5.9	6.2	6.6	6.5	7.0	7.7	7.8	8.2	8.4	8.8
	x100	47.2	13.5	11.5	10.6	10.6	10.8	12.0	12.7	13.3	13.7	15.2	16.1	17.2	18.2	19.1	19.8	20.7	21.3	22.1	23.4
2	x1	49.6	8.3	4.4	3.2	2.8	2.6	2.6	2.6	2.6	2.6	2.7	2.7	2.8	2.9	3.0	3.2	3.2	3.4	3.5	3.5
	x10	48.5	9.6	6.0	5.2	5.1	5.2	5.2	5.4	5.5	5.8	6.4	6.7	7.0	7.2	7.6	8.0	8.3	8.7	9.0	9.3
	x100	51.5	14.8	11.8	11.5	11.5	12.0	13.1	14.0	14.4	15.3	16.1	16.8	18.5	19.3	20.1	21.3	22.3	23.1	23.4	24.5
2.5	x1	53.0	9.2	4.5	3.3	2.8	2.7	2.6	2.6	2.6	2.6	2.7	2.8	2.7	2.8	2.9	3.0	3.2	3.4	3.5	3.6
	x10	53.8	10.6	6.3	5.4	5.1	5.2	5.3	5.5	5.7	6.1	6.4	6.6	6.9	7.3	7.5	8.2	8.4	8.7	9.0	9.4
	x100	56.6	15.8	12.9	11.9	11.9	12.4	13.1	14.3	14.7	15.2	16.3	17.0	18.9	19.3	20.1	21.2	22.2	22.7	23.6	24.1
3	x1	55.1	9.3	4.7	3.3	2.9	2.6	2.5	2.5	2.5	2.5	2.6	2.6	2.7	2.8	2.9	3.0	3.0	3.2	3.4	3.4
	x10	55.7	10.5	6.3	5.3	5.2	5.3	5.2	5.4	5.6	5.7	6.0	6.4	6.6	6.9	7.1	7.9	8.1	8.5	8.7	8.9
	x100	60.1	16.0	12.8	11.7	11.7	12.3	12.7	14.0	14.1	14.6	15.8	16.5	17.6	18.6	19.5	19.9	21.0	21.3	22.0	22.9

Table 6: The detection threshold to resolve a uniform disk spatially extended sources using two years of data for sources of varying spectral index and extension against varying background levels with different energy ranges. The upper table is the sensitivity when using photons with energies from 1-100 GeV and the bottom table is when using 10-100 GeV photons. The first column is the extended source's spectral index. The extended sources were simulated against a Sreekumar-like isotropic spectrum and the second column is the factor that the simulated background was scaled by. The remaining columns are varying sizes of the source's spatial model. The table quotes fluxes in units of 10^{-10}ph/cm^2/s. These values are also plotted in figure 23. More information about this table is presented in section 4.